UNIVERSITY OF GRONINGEN

Master Thesis :

A Coarse-Grained Molecular Dynamics Study of Complex Coacervation in Double Networks Hydrogels

Akbar Elnanda
s4199944
m.a.elnanda@student.rug.nl

February 10, 2025

University of Groningen

A Coarse-Grained Molecular Dynamics Study of Complex Coacervation in Double Networks Hydrogels

Master's Thesis

To fulfill the requirements for the degree of Master of Science in Physics

at the University of Groningen under the supervision of

Dr. A. Giuntoli (Zernike Institute of Advanced Materials, University of Groningen)

and

Prof. Dr. Ir P. R. Onck (Zernike Institute for Advanced Materials, University of Groningen)

and daily supervision of

Nayan Vengallur

Muhammad Akbar Elnanda Dzulfikar (s4199944)

February 10, 2025

Contents

1 Introduction

Hydrogels are three-dimensional networks typically constructed from crosslinked polymer chains, and featured with ability to absrob a large amount of water[1]. This water-absorbing capacity influences their structural properties, particularly their mechanical strength[2]. Recently, hydrogels have shown many attractive features that suit biomedical applications. For example, their water-rich composition allows them to mimic several parts of the human body composed of soft tissues[3]. Additionally, the composition of crosslinked macromolecules and water allows hydrogels to undergo reversible volume changes by absorbing and releasing liquid content[4]. These changes can be controlled by various stimuli, such as temperature, pH, ionic strength, and chemical reactions[5, 6, 7, 8]. As a result, hydrogels can be synthesized for specific biomedical applications [9].

Due to their ability to resemble the soft tissues of the human body, research on the biomedical applications of hydrogels has intensified. Studies range from investigating their mechanical properties, such as those relevant to tissue engineering, to their chemical properties, including applications in drug delivery and water absorption. However, recent studies show that conventional hydrogels, which are usually constructed from a single network (SN) polymer, exhibit soft and brittle properties. Thus, they do not meet the mechanical strength requirements for biomedical applications. For example, conventional hydrogels fail under tensile stress below sub-MPa levels and strain below 100%[4], whereas cartilage, as an example of soft tissue, has a fracture stress of 36 MPa[10].

Many attempts have been made to enhance mechanical properties of hydrogels. The toughness of a gel can be enhanced by introducing energy-dissipating mechanism[11]. Several works have been done to accomplish this mechanism. Henderson et al.[12], who worked on a gel with a copolymer of triblock chains, constructing the end blocks of different chains to form glassy domains, as well as their midblocks of different chains to form ionic crosslink. Tuncaboylu et al.[13] focused on the hydrophobic association that can influence the energy-dissipating mechanism. To achieve higher mechanical strength, Sun et al.[11] synthesized a tough hydrogel by mixing two types of crosslinked polymer composed of ionically crosslinked alginate and covalently crosslinked polyacrylamide. Among of the methods in order to enhance mechanical properties of hydrogels, the most prominent method is the double network (DN) scheme introduced by Jian Ping Gong[4].

The Double Networks (DN) hydrogel is a system in which two polymer networks with different properties are arranged to enhance the mechanical properties of the hydrogel itself. Basically, the first network in the DN is rigid and brittle, whereas the second networks is soft and ductile. The main idea of this scheme is to mitigate the fracture of the first network through the presence of the second network. Several examples of the rigid and brittle network that can be a good candidate for the first network are including Poly(2-acrylamido-2-methylpropanesulfonic acid) (PAMPS)[14], as the class of polyelectrolyte (PE)[14], highly crosslinked Polyacrylamide (PAAm), and Poly(ethylene glycol) diacrylate (PEGDA)[15]. Among the candidates of the first networks, polyelectrolyte complexes (PECs) have shown promising properties for biomedical application such as rapid self-assembly, responsiveness to stimuli, and tunable mechanical properties[16]. PEC hydrogels also exhibit mechanical stability due to high binding strength of electrostatic association above 5 $\varepsilon k_B T$[17]. PEC hydrogels allow dialysis to remove mobile counterion that can weaken electrostatic interactions. This process enhance mechanical properties since oppositely charged polymer are brought closer thus increase the binding strength of electrostatic interactions[18].

With polyelectrolytes acting as the first network, the DN can be synthesized through coacervation, a process that involves liquid-liquid phase separation. Hydrogel synthesis based on coacervation offers several advantages, including highly modular synthesis, highly efficient ionic interactions, and, most importantly, the sensitivity of coacervation to external stimuli such as polymer concentration, pH, and salt concentration, which makes its process and the resulting mechanical properties controllable[19]. Experimentally, many works have been done in investigating the mechanical properties of hydrogels based on coacervation. Lalevee et al.[20] studied the coaceravation formed from hyaluronic acid (HA) and chitosan (CS) where its mechanical properties are controlled by the dialysis pH. However, despite their success in creating strong and stretchable HS-CS hydrogels, they found that these properties were not preserve at pH beyond 3.0. In the work done by Wu et al.[21] the coacervation of polyvinylamine (PVAm) nanocrystalline domain was formed in PVAm-dense phase, incorporating the hydrogel with strain-stiffening properties.

Employing the tunable properties of coacervation, this work investigates the effect of the both networks architectures on the coacervation of the double networks hydrogel via molecular dynamics (MD) simulation. In the experiment, factors influencing the mechanical properties of hydrogels, such as the structure and conformations of polymer, are analyzed using small-angle neutron scattering (SANS), small-angle x-ray scattering (SAXS), and transmission electron microscope (TEM)[21]. While these techniques provide quantitative data, MD simulations offer insight into polymer behavior at the molecular level. Additionally, MD simulations also provide visualization of dynamics and interaction of the polymer.

The simulation in this work was performed in a coarse grained (CG) model, where atomistic systems are represented in fewer degree of freedom[22]. Since the degrees of freedom are reduced, simulations of larger spatial and temporal scales compared to atomistic models become achievable. In a CG model, complex atomistic-scale details are distilled into a more manageable form, yet it can still retain the key physical features of the system, preserving essential structural and interaction information[23]. In summary, CG models strike a balance between simplicity and the ability to capture critical system behavior.

Previous work carried out in this research group successfully confirmed the formation of granular structure within hybrid hydrogels, composed of poly(4-styrenesulfonate) (pSS) - poly(diallyldimethylammonium chloride) (pDADMAc) as PEC of the first network and polyacrylamide (pAAm) as as the second network, through CGMD simulations[24]. A "crowding"-induced liquid-liquid phase separation (LLPS) is observed from the decrease in the measurement of surface area of the PE, indicating complex coacervation occurs. The simulation reveals the interpenetration of the PEC network and the PAAm network, which is further confirmed as a contributing factor to the enhancement of hydrogel toughness.

In this work, the polymer sizes of PE and PAAm are varied to investigate coacervation under different structures of composing networks. The varying lengths of PE will provide insight into how the structure of PE influences the formation of coacervates. The varying lengths of PAAm, associated with the 'crowder,' will reveal the extent to which the presence of the crowder affects the motion of PE during complexation.The surface area measurement is used to evaluate the degree of coacervation. The radius of gyration, mean squared displacement, and radial distribution function are employed to characterize the behavior of PE during coacervation. Additionally, tensile testing is performed to provide insight into the effect of different constructed networks on the mechanical properties.

This work has found that a higher degree of coacervation is achieved with shorter PE chains. Short PE chains also exhibit higher mobility compared to longer chains. Charge fractions are also introduced, as a fully charged system does not support network interpenetration. However, lower charge fractions reduce the rigidity of the first network.

2 Background

2.1 Basics of Hydrogels

Hydrogels are networks constructed by cross-linked polymer chains and contain a high amount of water. The hydrophilic groups in the polymer networks enable hydrogels to swell in aqueous media[1]. This water-swollen property makes hydrogels a suitable candidate for several biomedical applications. In addition, hydrogels also offer advantages including enhanced biocompatibility, adjustable biodegradability, and porous structure[25].

According to Ho et al.[1] hydrogels can be formed from natural, synthetic, and the combination of both natural and synthetic polymer, called semi-polymer hydrogels. Despite the fact that natural hydrogels such as collagen, agarose, gelatin, fibrin, chitosan, and cellulose are biocompatible, biodegradable, and bioactive, they exhibit weak stability in terms of maintaining their structure and have lower mechanical strength compared to synthetic hydrogels[1]. Synthetic hydrogels, created from synthetic polymers such as polyethylene oxide (PEO), polyethylene glycol (PEG), polyvinyl alcohol (PVA), polyacrylic acid (PAA), and polyacrylamide (PAAM), exhibit controllable physical and chemical properties, although only a few of them are biocompatible[26]. As a combination of natural and synthetic polymers, semi-synthetic polymers are featured with bioactive characteristic of natural hydrogels and highly tunable properties through their varying chemical parameters.

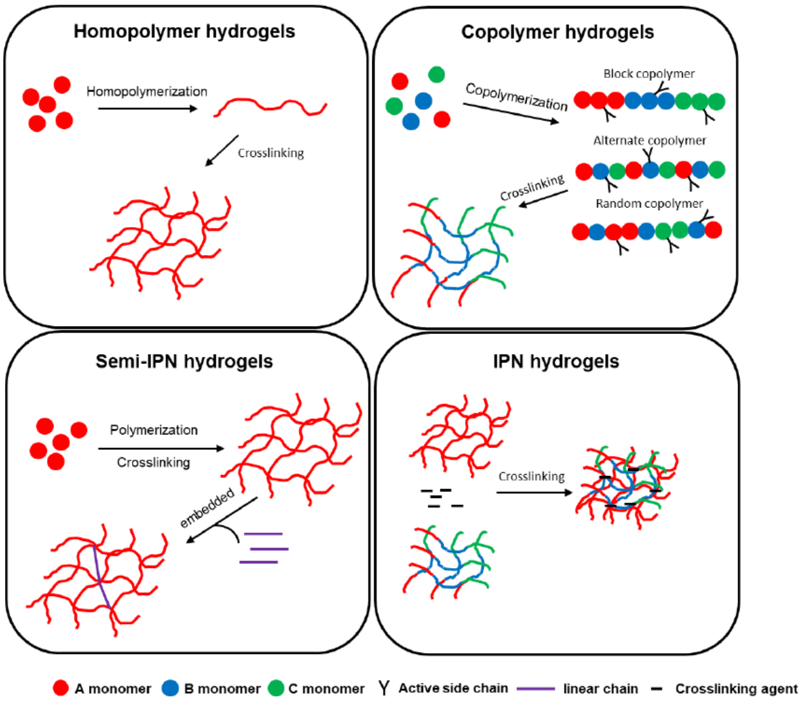

Figure 1: Simple diagram of homopolymer, copolymer, Semi-IPN, and IPN hydrogels, adapted form reference [1]. Homopolymer hydrogels (top-left) are constructed from the crosslinked of one type monomer in polymer chain, whereas copolymer hydrogels (top-right) are constructed from the crosslinked of different type of monomer in polymer chain. In semi-IPN hydrogels (bottom-left) polymer networks are embedded in linear polymer chains, whereas IPN hydrogels are formed from two or more polymer networks.

Hydrogels can be constructed by several types of polymer such as homopolymer, copolymer, interpenetrating polymer network (IPN), and semi-IPN [1]. A homopolymer is formed by one type of monomer arranged in a chain, whereas a copolymer is composed of two or more types of monomers that can be arranged in block, alternating, or random configurations. In copolymer hydrogels, the active sides of each chain can cross-link to neighboring chains. Both homopolymer and copolymer hydrogels consist of one type of polymer chain. In contrast, two or more types of polymer chains form both IPN and semi-IPN hydrogels. IPN hydrogels are formed from two or more polymer networks that cross-linked via crosslinking agents, whereas semi-IPN hydrogels do not utilize crosslinking agents. Instead, this type of hydrogel consists of polymer networks embedded within the linear polymer chain without the use of crosslinking agents.

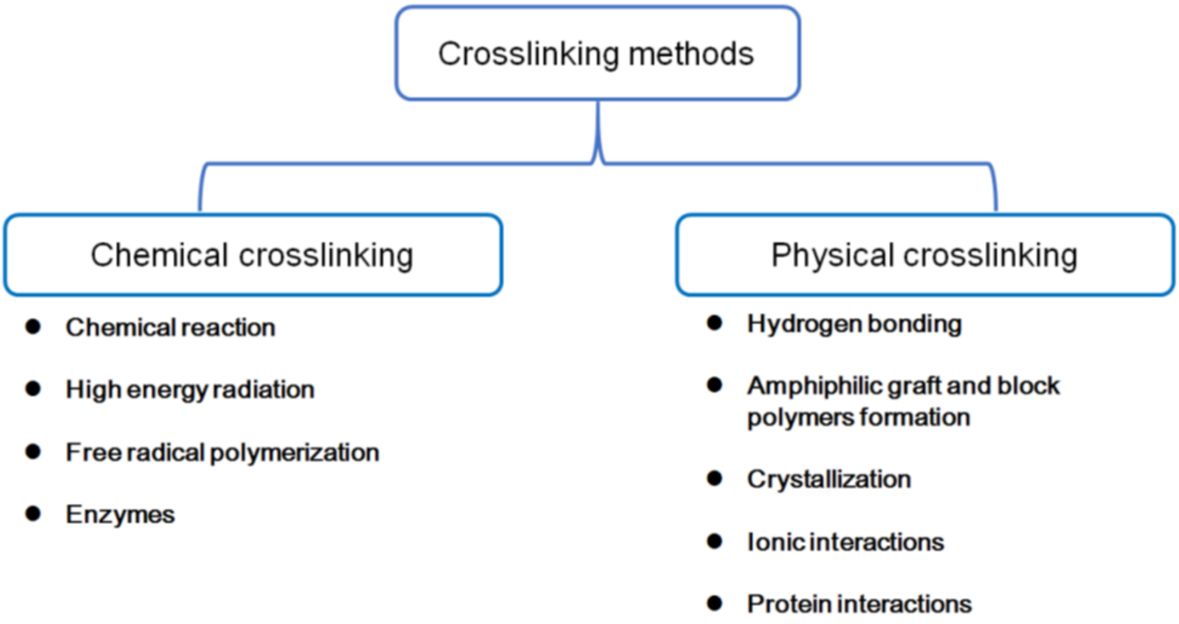

Figure 2: Methods that can be utilized in to create crosslink in polymer networks, adapted from reference [1]. Physical crosslinkings are generally weaker compared to chemical crosslinkings.

Based on the crosslinking method, there are two types of hydrogels: chemical and physical hydrogels. They are distinguished by the type of junction connecting the network. The networks in chemical hydrogels are connected by permanent junctions composed of crosslinking from covalent bonds and polymerizing end-functionalized macromolecular monomers. In physical hydrogels, the junction is temporary and composed of physical interaction like hydrogen bonding, ionic interaction, and crystalization[27]. Hence, beside having weaker mechanical properties compared to chemical hydrogels, physical hydrogels also have reversibility from liquid to solid[28].

Double Network (DN) hydrogels are classified as either IPN or semi-IPN and exhibit excellent mechanical properties based on an internal fracture mechanism[4]. For example, in terms of fracture energy G, a single network (SN) of polyacrylilamide gel (PAAm) has $G \approx 1 J/m^2$, while poly (2-acrylamido, 2-methyl, 1-propanesulfonic acid) polyelectrolyte (PAMPS) has $G \approx 0.1 J/m^2$[29].Surprisingly, when the two are combined, they show a notable increase in fracture energy, approximately 100 to 1000 times higher[30].

The remarkable mechanical properties of the DN arise from the interactions between the forming networks. Some possibilities for illustrating the interactions between networks have arisen. Nakajima et al[31] speculated that the fracture in the brittle first network is mitigated by the soft second network through a force transfer mechanism. The effect of the entanglement between the networks was also suspected to enhance the strength of the DN[32]. From a molecular point of view, using small-angle neutron scattering and viscosity measurement, Wu et al.[33] found that the interactions between PAMPS and PAAm are stronger than their interaction with water. Conversely, Brown made an assumption that the fracture process of the first network triggers a cross-linking reaction between the two networks[34].

The strength of the DN is also influenced by several factors. Gong found that the molecular ratio between the first and second networks plays a crucial role in determining the strength of the DN. The strength of the DN increases as the molar ratio of the second network to the first network also increases[4]. Besides the ratio, the strength of the DN is also affected by the crosslink density of the second network. A higher crosslink density leads to a reduction in the strength of the DN[4]. Better visualizations are provide in figure 3

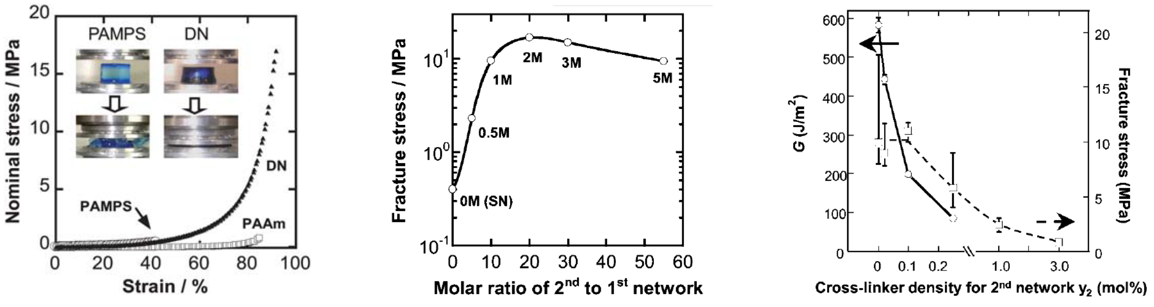

(a) (b) (c)

Figure 3: Mechanical properties are affected by DN network conformation, figure adapted from reference[4]. A compressive nominal stress-strain curve (a) of PAAMPS/PAAm DN(▲), SN PAMPS (○), and PAAm(□), shows a significant increase of DN system. The fracture stress of the DN (b) decreases as the molecular ratio of the second network to the first network increases. The mechanical strength, including fracture stress and fracture energy (c), is reduced as the crosslink density increases.

In terms of crosslink density, the behavior of mechanical strength can be better understood from transfer force mechanism. When a force is applied to the DN, the crosslinks in the second network act as anchors that transfer the force to the first network, leading to network fracture[31], as the scheme is shown in figure4

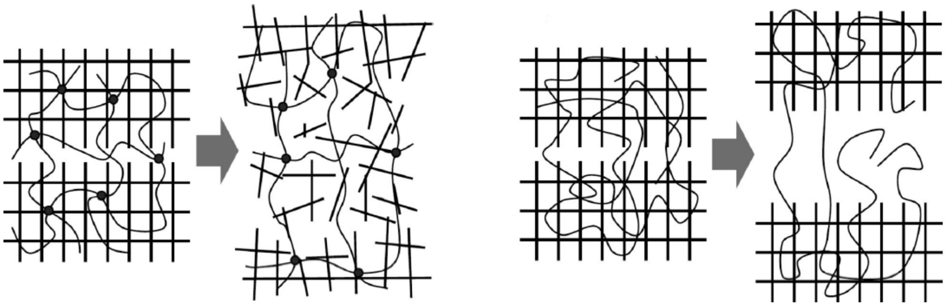

(a) (b)

Figure 4: The fracture process in two different DN systems, figure adpated from reference[31]. In figure (a) The crosslink points, indicated by black dots, in the second network act as anchors that transfer force during elongation. The forces are easily transferred to the first network from a crack created by elongation, leading to breakage of the first network in a wide range. Figure (b), in contrast, shows that linear second network are less likely to transfer force.

Therefore, as it is proposed by Gong, a good DN should satisfy these conditions

1. The first network should be rigid and brittle, whereas the second network should be soft and ductile.
2. The molar concentration of the second network should be higher 20-30 times than the first network
3. the first network should be tightly crosslinked, while the second network is loosely cross-linked, requiring a very high molecular weight for the second polymer.

Polyelectrolyte (PE) is one example of the widely used candidate for the first networks[4]. PE shows brittle nature due to the large osmotic pressure generated by dense counterions, causing significant swelling of the gels and leading to a stretched state of their polymer chains[35]. Meanwhile, the ductility of the second network is achieved through sparsely crosslinked neutral polymers, which provide high stretchability[30].

2.2 Mechanics of Networks

The mechanical properties of networks, such as elasticity, strength, and toughness, are highly influenced by molecular parameters accessible to the synthetic chemist or formulator, including the average density of cross-links and the effect of added fillers on experimental factors such as strain rate and temperature[36]. For example, to enhance stiffness, stress at break, and fracture energy while maintaining high extensibility, a dissipation mechanism is introduced into the networks[37],[11]. Hydrogels, as soft interpenetrating networks, employ the combination of stiffness and elasticity at small strains with minimal energy dissipation[36].

The elasticity of flexible chains in a network is directly depended on the conformational entropy of the molecules. In a crosslinked network, the crosslink points act as separators between strands; hence, the shear elastic modulus μ_x is defined as the sum of free energy of the strands[36].

$$\mu_x = \nu_x kT = \frac{\rho RT}{M_0 N_x} \tag{1}$$

where ν_x is the density of elastic strands[38], ρ is the mass per unit volume of the polymer, M_0 is the molecular weight of the monomer, and N_x is the number of monomer per chains.

In an incompressible material, if the modulus is known, the large-strain behavior can be approximated using a free energy function W in such a way

$$W = \frac{\nu_x k_B T}{2} \left(\lambda_1^2 + \lambda_2^2 + \lambda_3^2 - 3\right) \tag{2}$$

where λ_1^2, λ_2^2, and λ_3^2 are the principal stretches. Since soft materials are generally incompressible, their principal stretches are equal to 1. Therefore, in special case of uniaxial extension, equation2 yields the prediction for nominal stress as the function of stretch in such a way:

$$\sigma_N = \nu_x k_B T \left(\lambda - \frac{1}{\lambda^2}\right) \tag{3}$$

However, this prediction only holds at small and moderate strains for rubbers and hydrogels without entanglements[39].At high stress, the chains near their finite extensibility limit become significantly stiffer; hence, the finite extensibility parameter should be introduced in empirical models[36]. In the presence of both cross-links and entanglements, Rubinstein and Panyukov[40] proposed a model called the slip-link model, which provides a more accurate prediction of nonlinear behavior as long as the finite extensibility of the chains is not activated.

$$\sigma_N = \nu_x k_B T \left(\lambda - \frac{1}{\lambda^2}\right) - \frac{\nu_e k_B T \left(\lambda - \frac{1}{\lambda^2}\right)}{0.74\lambda + 0.61\lambda^{-0.5} - 0.35} \tag{4}$$

where ν_e is the density of entanglement. In the representation of the Mooney function, equation 4 can be rewritten in such a way

$$f^*(\lambda^{-1}) = G_c + \frac{G_e}{0.74\lambda + 0.61\lambda^{-0.5} - 0.35} \tag{5}$$

where G_c is modulus obtained from the model proposed by Rubinstein called phantom model [38]and G_c is entanglement modulus. The phantom modulus G_c can be redefined as

$$G_c = \big(1 - \frac{2}{\phi}\big)\nu_x k_B T \tag{6}$$

where ϕ is the functionality of the crosslinker. Equation 6 successfully revealed the behavior of SN gels that demonstrates an increase in fracture stress and a decrease in fracture stretch ratio with increasing ν_x[41].

In investigating the mechanical properties of the DN system, many studies have been conducted using both experimental and computational approaches. Experimentally, Jian Ping Gong in her works investigated the effect molar ratio between the first and second network on mechanical properties quantified by the fracture stress[4]. She found that good mechanical properties were achieved by tailoring the rigid network as the minor component and the soft network as the major component. The influence of chemical structure of crosslink density and its generation on mechanical strength was investigated by Nakajima et al[31], which resulting in a conclusion that the high crosslink density leads to a breakable network. Computationally, Higuchi et al.[42] performed a tensile test simulation of double networks in different proportions of the first and second networks, and different configuration of both networks, where they found that the tense first network increases Young's modulus.

2.3 Complex Coacervation

Complex coacervation refers to the process in which two oppositely charged molecules undergo associative phase separation[43]. Two phases, a dense phase (coacervate) and a dilute phase (supernatant), are formed during this process[44]. As a result of electrostatic interactions, two oppositely charged molecules are attracted to each other. When the total number of positive and negative molecules is equal, the attraction between them forms complexes, resulting in phase separation, whereas an inequal number of positive and negative molecules resulting in inhibited phase separation and increase solubility[45]. The aggregate complexes separate from the solution into a dense phase, that holds the majority of polymer, and a supernatant phase, which mostly contains water. This phase speration is also stabilized by the presence of non-covalent interactions such as hydrogen bonding and Van der Waals forces. In terms of electrostatic interactions, several factors can be applied to control the coacervation such as salt concentration, that affects ionic strength, and pH, that affects the charge density.

The earliest theory, well known from the Voorn-Overbeek theory[46], initiated a conceptual understanding of the competition between the translational entropy of the charged species and the electrostatic attractions between the same species. This theory involves the interaction of polyanion and polycation, as will be referred as polyelectrolytes, combines Flory-Huggins thoery of mixing for polymer solutions and the Debye-Huckle theory of dilute electrolyte[43].

$$\frac{F_{VO}}{Vk_BT} = \sum_i \frac{\phi_i}{N_i} \ln \phi_i - \alpha \left[\sum_i \sigma_i \phi_i \right]^{\frac{3}{2}} + \frac{1}{2} \sum_{ij} \chi_{ij} \phi_i \phi_j \tag{7}$$

The mixing entropy is specified in the first term on the right hand side and featured with volume fraction ϕ_i and the degree of polymerization N_i. The Debye-Huckel free energy is represented in the second term that is composed of the strength of electrostatic energy $\alpha = \lambda_B/2a$, where λ_B is the Bjerrum length and a is the radius of charged species. Here, σ_i indicates the balanced ratio between the number density and the volume fraction. Despite the original theory only considered the first two terms, the third term that involves short range interaction between species χ_{ij} is often included[43].

This model leads to a prediction that the complex coarcevation occurs at the low salt and polymer concentration. As is shown in figure 5, the predicted phase diagram agree with the standard Flory-Huggins phase diagram, except the y-axis is temperature rather than salt concentration. This finding proves that in the phase separation, salt concentration can weaken the driving force likewise temperature does in the standard χ-driven phase separation.

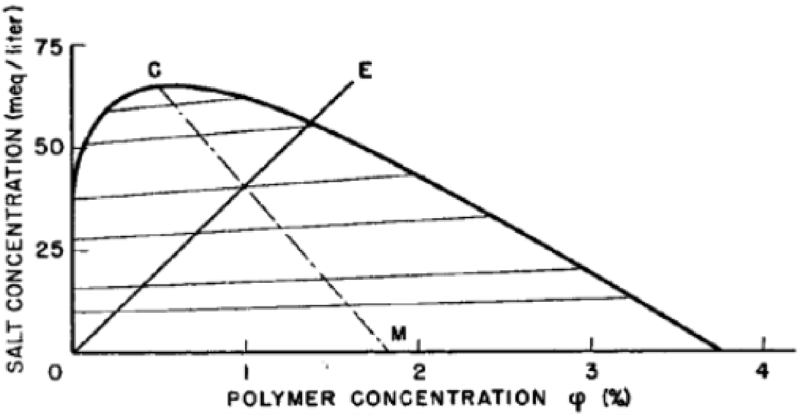

Figure 5: The phase diagram in terms of polymer concentration versus salt concentration predicted by Overbeek and Vorn[46]. The E line represents the the conditions where the salt concentration is completely composed of polyelectrolyte counterions. Point C indicates the critical point of salt concentration.

Although Voorn–Overbeek theory provides theoretical predictions for complex coacervation, several notes must be taken into consideration. According to Sing and Perry [43], Voorn-Overbeek theory does not work under conditions of high charge densities and high concentrations of the materials. This theoretical limitation arises from several factors. For instance, Debye–Hückel theory serves as a limiting law under conditions of low salt concentrations. The theory approximates the mean-field environment around a single salt ion by solving the linearized Poisson–Boltzmann equation[47]. Consequently, its thermodynamic predictions are only accurate for dilute, weak electrolytes, specifically monovalent salts at concentrations below 5 mM[48]. The polymer charges are also considered as unconnected particles, eliminating any structural distinction between salts and polymers[43] solvent is assumed to be a continuum. Additionally, Voorn–Overbeek theory assumes the solvent to be a continuum, accounting only for the relative dielectric constant in the Bjerrum length[43]. Meanwhile, solvent structure plays a crucial role in coacervate thermodynamics[49].

Despite its limitations, Voorn-Overbeek theory remains widely used because it qualitatively captures many aspects of coacervation[43]. Notably, studies by Spruijt et al. [50] have demonstrated that, with appropriate parameterization, the theory can successfully match experimental phase diagrams and interfacial tension data. However, in this work, Voorn–Overbeek theory has so far only succeeded in predicting phase behavior in the absence of additional agents[43]. Given the complexity of coacervation, numerous studies have been conducted to explore its behavior in the presence of other agents.

In a paper by Andre and Spruijt[51], which summarizes coacervation in biomolecular systems in the presence of other agents—later referred to as "crowders"—the authors highlight several factors that enhance coacervation. These include increased intermolecular attraction due to volume exclusion by crowders, direct interactions between crowders and phase-separating biomolecules, and reduced biomolecules solubility caused by crowders. The study by Bai et al.[52] investigated the coacervation of biopolymers and demonstrated that it can be regulated by adjusting the concentration of Bovine Serum Albumin (BSA), the crowder. Their findings show that BSA concentration influences phase distributions, morphologies, and the kinetics of incorporated biopolymers within the system.

As complex coacervation employs salt as the driving force, hydrogels based on polyelectrolyte complex coacervation facilitate structural tunability[53]. For example, in the work done by Hunt et al.[54], complex coacervation, resulting from the phase separation of ion-rich regions from the aqueous environment in ABA triblock copolyelectrolytes, successfully creates tunable supramolecular hydrogels. The study conducted by Zhang et al.[55] on the Hofmeister effect in the polyelectrolyte complex coacervation of DN hydrogels reveals that the presence of inorganic salts enhances the mechanical properties of the hydrogels. Additionally, to achieve the ideal structure of an interpenetrating double network, a recent study conducted by Es Sayed et al.[24] shows that the coacervation of polyelectrolytes influences the mechanical properties of hydrogels.

2.4 Coarse-Grained Molecular Dynamics

Molecular dynamics (MD) is a powerful simulation technique that can be utilized to investigate the physical and chemical properties of materials and biological molecules[56]. Despite quantum mechanics being well known for its reliability in studying molecular interactions, MD simulations are based on Newton's laws and focus on bulk properties, which do not depend significantly on small-distance behaviors. MD simulations typically involve a large number N of particles that start in a predefined configuration and equilibrate into a dynamic state, while incorporating a microcanonical ensemble in statistical mechanics, where energy E, volume V, and the number of particles N remain fixed[56].Since the velocity and position of each particle change continuously, the motion of each particle has to be followed up in a certain time in order to determine its effect on other particles, which are also moving. Newton's law are applied with assumption that the net force on each molecules is the sum of the two-body forces with all other $(N-1)$

molecules[56]. After the simulation has run long enough to stabilize, The average of the dynamics quantities is computed in order to compute thermodynamics properties.

$$m\frac{d^2\boldsymbol{r}_i}{dt^2} = \sum_{i<j=0}^{N-1} \boldsymbol{f}_{ij}, \quad \text{where} \quad i = 0, ..., (N-1) \tag{8}$$

The reliability of the outputs of MD highly depends on the number of molecules N involved in the simulation, according to equation 8. Besides improving statistical accuracy and reducing finite-size effects[57], a large N also better represents energy and momentum exchange processes, ensuring proper thermalization and equilibrium distributions[58]. Additionally, a large N better represents thermodynamic behavior and accurately models bulk properties such as density, viscosity, and diffusion[57]. However, this would be computationally expensive and inefficient. Generally, in investigating the properties and behavior of soft materials such as gels, colloids, and polymers, an all-atom (AA) model is employed in MD simulations, which is quite large and computationally demanding[22].

To tackle the challenge in terms of efficiency, a corse-grained (CG) model is proposed. the CG simulations model the system in a fewer degree of freedom[22]. From the MD point of view, CG models are composed of interacting mass points (CG) where each of it represents a group of atom from AA simulation in the same system. Therefore, CG can be regarded as relatively low-resolution models that are fairly consistent with their more detailed AA models. Due to their fewer degree of freedom, fewer particles are computed, hence larger integration time steps are allowed.

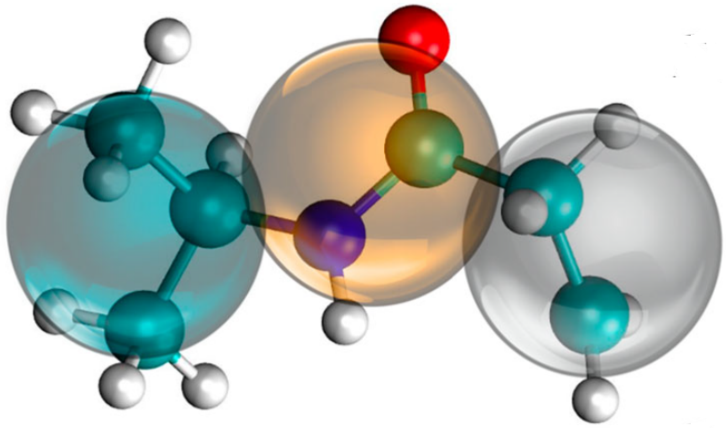

Figure 6: A CG model of polymer, adapted from reference[22]. Monomers of the same system are grouped into one bead, reducing the order of particle representation.

According to Joshi and Desmukh[22], Coarse-grained models are basically divided into three categories. First, those that reduce the order of particle representation in molecular structures. Second, those that assume atomic-scale homogeneous deformation. Lastly, those that utilize *field* representations. The coarse-grained methods that model soft-matter MD usually are based on reduced-structure methods, and they encompass two critical steps, including mapping of CG beads onto the atomistic structure of molecules and development of force field (FF) that define the interactions between CG beads.

In CG mapping, AA model simplified by grouping atoms into larger representative units called CG beads[22]. The choice of mapping schemes and the degree of coarse-graining must balance accuracy and computational efficiency while preserving essential physical and chemical properties[59]. Different mapping approaches are used based on molecular characteristics, such as polymer tacticity[60] or ring geometries[61]. Additionally, for explicit solvent models, which may provide an actual representation of the experimental conditions, the interactions of solvent-solvent and solvent-solute are important[62]. Since CG mapping should minimize statistical correlations between internal degrees of freedom, allowing bonded interactions to be treated separately as bond stretching, angle bending, and torsion[63], CG bead centers are chosen to ensure that the bonds between them can be modeled using a single harmonic potential[64].

After mapping, force-field (FF) parameters governing the interactions between CG beads are introduced. There are three types of FF parameters: the Bottom-up approach, the Top-down approach, and the hybrid approach[22]. In the Bottom-up approach, the FF parameters are adjusted by reproducing microscopic thermodynamics and structural properties obtained from atomistic simulations[65]. Although the bottom-up approach relies on an accurate atomistic model to be effective, it is valuable for predicting unknown microscopic quantities due to its foundation in statistical mechanics[64]. However, in the complex many-body potential of mean force (PMF), the bottom-up approach makes approximations, resulting in limited transferability and accuracy of macroscopic thermodynamic predictions[66]. Different from the bottom-up approach, the top-down approach reproduces macroscopic experimental phenomena observed at length scales accessible to CG models to tune the CG parameters[22]. Since the top-down CG models are designed to replicate macroscopic phenomena, the measured microscopic properties may not be accurate, but a high degree of transferability is provided[67]. The hybrid approach is a combination of both the bottom-up and top-down approaches, modeling bonded interactions based on microscopic structural properties, and non-bonded interactions to replicate macroscopic phenomena, enabling the replication of microscopic properties with considerable transferability[22].

In general, after molecules of AA level are mapped into CG beads, the interactions between the beads can be defined as bonded and non-bonded contributions.

$$U_{total}^{CG} = \sum U_{total}^{bond} + U_{non-bond}^{CG} \tag{9}$$

The bonded interactions usually can be modelled by several empirical potential such as Morse[68], Finite Extensible Non-linear Elastic (FENE)[69], and Harmonic potential. As example, Harmonic potential that is the most commonly used follows an expression

$$U_{bond} = K(r - r_0)^2 \tag{10}$$

where K is the bonded force constant and r_0 is the equilbrium bond length. For angles potential, several potentials are the most commonly used including harmonic[61], cosine harmonic[70], and Fourier angle[71]. As example, harmonic angle potential can be written in an expression:

$$U_{angle} = K_\theta \left(\theta - \theta_0\right)^2 \tag{11}$$

where, K_θ is the angle force constant and θ_0 is the equilibrium angle. The torsion potentials are formed from the combination of dihedrals and impropers and depend on a set of four CG beads[22]. The most common empirical potential forms for dihedrals and impropers are cosine and harmonic respectively given by:

$$U_{dihedral} = K_\varphi \left[1 + \cos(n\varphi - \varphi_0)\right] \tag{12}$$

$$U_{improper} = K_{\Phi} \left(\Phi - \Phi_0\right)^2 \tag{13}$$

Here, K_{φ} and K_{Φ} represent the force constants, while φ_0 and Φ_0 are the equilibrium dihedral and improper angles, respectively. The value of n denotes the multiplicity, which indicates the number of minima as the bond rotates.

The non-bonded interactions include coulombic and Van der Waals interaction. The coulombic interaction is expressed using Coulomb's law, whereas Van der Waals interaction is described by Lennard-Jones (LJ) potentials. All the details of utilized potentials will be further discussed in the methods section.

3 Methods

3.1 The System

3.1.1 Model

The simulations of the DN in this system were performed in a coarse-grained molecular dynamics (MD) model, whereas a bead represents a group of monomers whose behavior is governed by the same interactions. Consequently, one bead corresponds to a Kuhn length segment of the polymer. The system was modeled in the Kremer-Grest beads spring model in the Lennard-Jones units and comprised of many potentials to govern specific interactions of the beads such as Lennard-Jones potential, harmonic bond potential, FENE potential, soft potential, and a Coulombic potential. There are three stages of simulation in creating the coarcevation system: the equilibration, the cross-linking, and the desalting protocols. Each potential was utilized in specific protocols. Additionally, a tensile test simulation were performed to gain insights on how the structure of the network influence it mechanical properties.

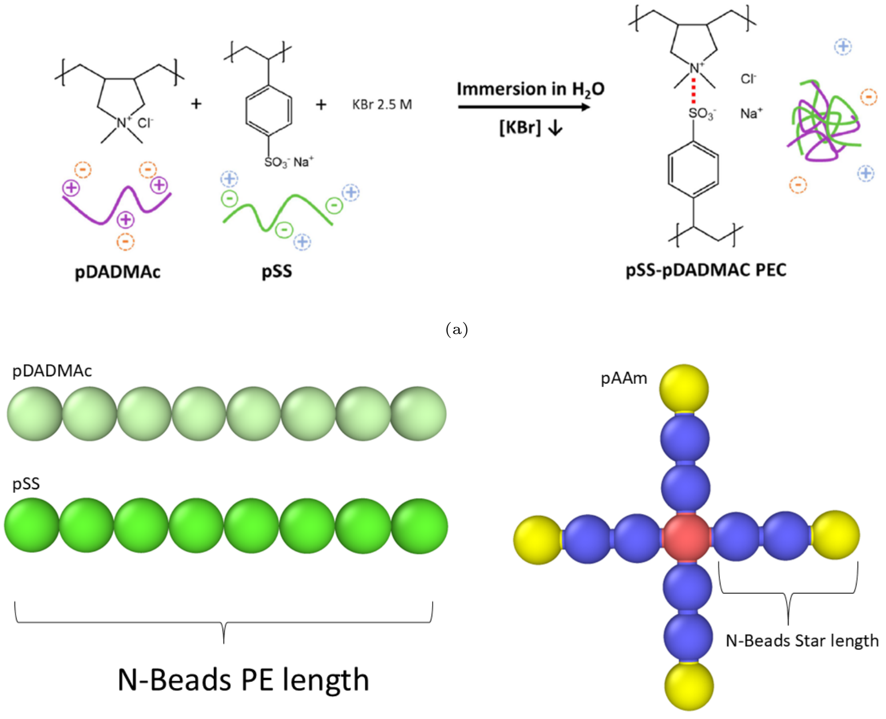

(a)

(b)

Figure 7: (a) Schematic reaction of polyelectrolytes by Es Sayed et all.. [24] One bead represents a Kuhn length segment of the polymer. The first network are constructed from PE composed of pDADMAc and pSS, whereas the second network is formed from neutral pAAm (b) Structure of polymer chains modeled in the simulation.Polyelectrolytes are depicted as linear chains, whereas pAAM takes the form of a telechelic star, enabling it to construct a crosslinked network during the crosslinking process. The yellow beads of pAAm represent the reactive end beads of polymer chain that will create the bond to other telechelic stars thus it constructs corsslink point

In this simulation, the DN is constructed from PE composed of poly(4-styrenesulfonate) (pSS) and poly(diallyldimethylammonium chloride) (pDADMAc) as the first network, and polyacrylamide (pAAm) as the second network. One bead represents a Kuhn length segment of the polymer. Since the simulations were performed in LJ units, the mass and the diameter of each beads were quantified in LJ units as well. All the beads were set to have the same mass and diameter of 1 m_{LJ} and 1 σ_{LJ} respectively. However, after the simulation of equilibration protocol, the beads of pSS and pDADMAc were set to have different charges 1 and -1. Both pSS and pDADMAc were structured as linear polymer chains that will aggregate as a result of coulombic interaction, whereas pAAm was structured as telechelic stars. For bonded interactions, the chains possess an angle potential $U_{angle} = K_\theta[1 + \cos(\theta)]$. The K_{PE} was set to $K_{PE} = 4$, to ensure moderate chain stiffness of PE. The number of salt beads of opposite monovalent charges was added accordingly to prevent coacervation to occur before the pAAm networks were constructed via the cross-linking protocols.

In order to simulate good solvent conditions, non-bonded interactions are governed by the standard LJ potential and Coulombic potential, noting that the simulations are performed in the charged system. Here, implicit solvent models are utilized where the solvent is treated as a continuum that interacts with the solute through a dielectric constant and other parameters. The standard LJ potential follows the equation:

$$U_{LJ} = \begin{cases} 4\epsilon\left[\left(\frac{\sigma}{r}\right)^{12} - \left(\frac{\sigma}{r}\right)^{6}\right] & \text{for } r \leq r_c \\ 0 & \text{for } r > r_c \end{cases} \tag{14}$$

whereas $\epsilon_{LJ} = 1$ is the interaction strength, $\sigma = 1$ is the LJ beads of size, and cutoff $r_c = 1.12\sigma$.

The interactions of each beads follow Coulombic potential in such a way:

$$U_{coul} = \frac{Cq_iq_j}{\epsilon r} = -\frac{Ce^2z^2}{\epsilon r} \tag{15}$$

where C is an energy-conversion constant, q_i and q_j represent the charge of the two atoms, r is the distance between two atoms, and ϵ is the dielectric constant of medium. Through this equation, the ratio of this energy to thermal energy k_BT can be written in expression

$$\frac{\beta e^2z^2}{\epsilon r} = z^2\frac{l_B}{r}, \quad \text{where} \quad \beta = \frac{1}{k_BT} \tag{16}$$

which gives us the expression of *Bjerrum Length*

$$l_B = \frac{e^2}{\epsilon k_BT} = \frac{e^2}{4\pi\varepsilon_0\varepsilon_r k_BT} \tag{17}$$

where ε_0 is the vacuum's permittivity and ε_r is the solvent's relative permittivity. Bjerrum length can be defined as the length where the Coulomb energy between two units is approximately comparable with the thermal energy k_BT[72].

The long range coulomb interactions were calculated via particle-particle particle-mesh style where the charges of atom are mapped to a 3d mesh. In this method, the 3d FFTs is applied to solve Poisson's equation on the mesh, then electric fields on the mesh are interpolated back to the atoms [73]. The relative errors of this calculation was set 10^{-4} and the cutoff radius of long range coulombic interaction is $r_c = 10\sigma_{LJ}$.

3.1.2 Network Parameters

The DN in this system was modeled to have a concentration of 10% of the total concentration. This was achieved by setting the number of beads in the DN to approximately 41000 beads and the box length to 74 length units. The fraction of the first and second networks was maintained to 30:70, leading to the 12000 and 29000 beads of the first and second networks, respectively. The 12000 beads of polyelectrolyte composed of the same number of beads of polycation and polyanion require 170000 of total monovalent salts in equal number to prevent aggregation due to coulombic interaction. The boundaries of the simulation box were set periodic. The positions and velocities were updated in the Velocity-Verlet algorithm with integration time step $\delta t = 0.005\tau_{LJ}$, where $\tau_{LJ} = (m_{LJ}\sigma_{LJ}/k_B T)^{1/2}$ and the thermal energy was set to $k_B T = 1.0$

Table 1: The number of each component constructed the system

Component			Number	Unit
Network	1st	pSS	6000	N-Beads
		pDAD-MAc	6000	
	2nd	pAAm	29000	
Salt		cation	85000	
		anion	85000	
Simulation box volume			74^3	σ_{LJ}^3

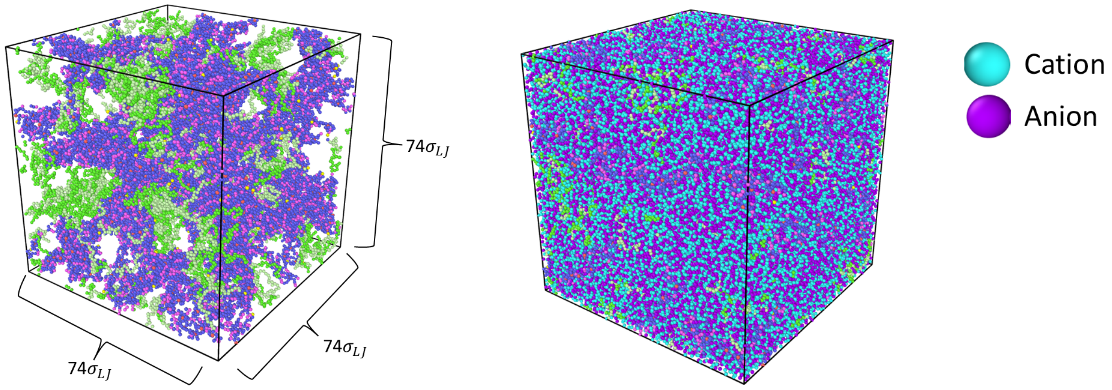

(a)

(b)

Figure 8: (a) A snapshot of the system without salts. The green beads represent the polyelectrolyte network, whereas the blue beads represent the cross-linked telechelic star of pAAm network. The proportion of pAAm and PE was maintained to 70:30. The box length was set to $74\sigma_{LJ}$. (b) A snapshot of the full system. 85000 beads of both cation and anion were required to prevent aggregation of polyelectrolyte.

In order to investigate the effect of architecture of the systems, the length of both networks were varried, while the total numbers of each component were maintained approximately the same. The number of arms in the telechelic star was also varied between 4 and 6, as shown in Figure 9. Increasing the number of arms enhances the functionality of telechelic stars in creating crosslinking points. Each modeled system was simulated in three independet replica with different initial velocies.

Table 2: Variation of structure in this work

Parameters	**Quantities**	**Unit**
Star arm length	2, 4, 8, 16, 32	Beads
Polyelectrolyte length	50, 75, 100, 125, 150	Beads
Number of arms of the star	4, 6	N

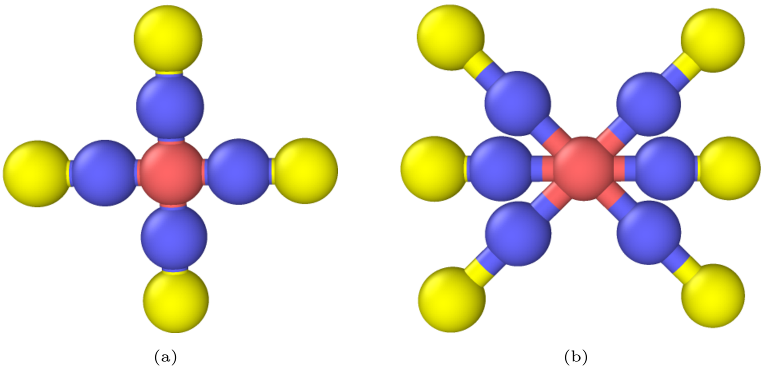

Figure 9: Telechelic stars with 4 arms (a) and 6 arms (b). The main idea behind adding more arms is to increase the number of crosslinking points in the neutral network.

3.1.3 Chain parameters of Polyelectrolyte Density

In the variation of the charge density in the PE chains, the numbers of charged beads were varied accordingly to satisfy a fraction of 80% to 20% in the decrement of 20%. To model this, a single chain of PE composed of 10 beads was created. The 80% charge fraction means that within a chain of 10 beads, 8 beads are charged and the rest are not. The uncharged beads are positioned accordingly; thus, they are distributed equally along the chain to avoid the effect of blockiness. The chain is replicated according to the total length of PE required.

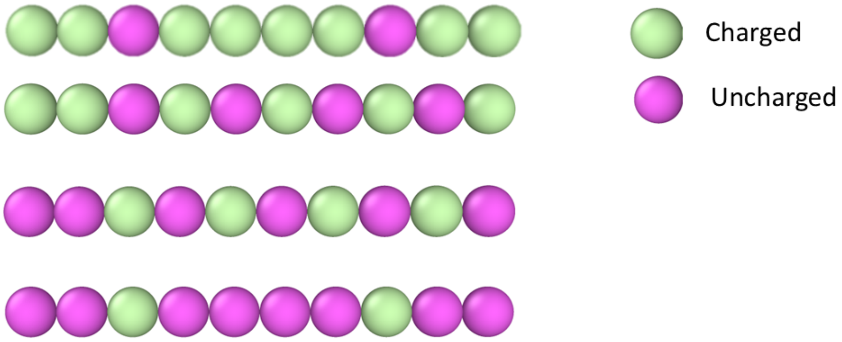

Figure 10: The model of charge fraction from 80% (top) to 20% (bottom). The green beads represent charged beads, whereas the pink beads represent uncharged beads of polymer chain

3.2 Simulation Stages

In this work, the system had to undergo three simulation protocols: the initial equilibration, cross-linking, and desalting.

3.2.1 Equilibration

In the initial equilibration protocols, the charge of the beads was set to be off. In the first stage of this protocols, a relaxation process was simulated. The bonds of each beads was set to have a harmonic style with potential

$$E = K(r - r_o)^2 \tag{18}$$

where $K = 2500$ and $r_o = 9$. The inter-chain beads interaction was governed by soft potential

$$E = A\left[1 + \cos\left(\frac{\pi r}{r_c}\right)\right] \quad \text{for} \quad r < r_c \tag{19}$$

This potential is useful for to prevent atoms to overlap, thus it will not blow up as r goes to 0. A is an energy units which was varied to 0 at the first step of simulation and 300 as the timestep of the relaxation ended. The cutoff distance was set to $r_c = 1$. This relaxation was performed in the canonical (NVT) ensemble via Nose-Hoover thermostat for $1 \times 10^4 \tau_{LJ}$ time step. After relaxation ended, the simulation box was shrunk to the targeted length, then equilibrated again in the NVT for $3 \times 10^6 \tau_{LJ}$ more.

3.2.2 Crosslinking

The charge of the beads was turned on in the crosslinking protocols. A finite extensible nonlinear elastic (FENE) [69] potential was applied to govern the bond interactions in the chain

$$E = -0.5KR_0^2\left[1 - \left(\frac{r}{R_0}\right)^2\right] + 4\epsilon\left[\left(\frac{\sigma}{r}\right)^{12} - \left(\frac{\sigma}{r}\right)^6\right] + \epsilon \tag{20}$$

The first term is attractive, the second term is repulsive. The parameters were set to $K = 30k_BT/\sigma_{LJ}^2$, $R_0 = 1.5\sigma_{LJ}$, $\epsilon = 1.0$, and $\sigma = 1\sigma_{LJ}$.

The crosslinks were created if the beads on the very edge of the arm of telechelic star were closer than $1.12\sigma_{LJ}$ using fix/react command on LAMMPS. The simulation was performed until the degree of curing reach above 92%, then it was re-equilibrated in NVT ensemble for $1 \times 10^6 \tau_{LJ}$. Noting that the total number of the beads is maintained the same, short star polymer (SP) length results to a high crosslink density and vice versa.

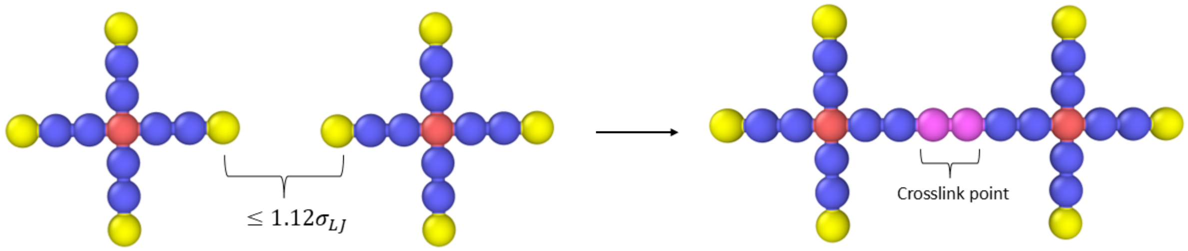

Figure 11: Crosslinking reaction of two close telechelic stars. The two close neighboring beads created a bond and became crosslinking point, indicated by pink beads

3.2.3 Desalting

As the last stage in creating the system, the equal number of cation and anion salts were removed gradually. For every $1000\tau_{LJ}$, 200 cations and anions were removed. The process was performed until the salt ions were completely removed. After desalting finished, the system underwent equilibration for $5 \times 10^6 \tau_{LJ}$ time step.

3.2.4 Tensile Test protocols

The tensile test protocols were performed on several samples as follows: using the same PE length with different star arm lengths. The aim of the first method is to investigate how the length of PE affects the mechanical properties of the network. Simulations were performed along three different axes for each sample until the network was stretched to seven times its initial length. The final result represents the average across the three axes for each sample, with each sample having three replicas.The bonds in the chain break when the chains are strained such that their bond lengths stretch beyond $1.35\sigma_{LJ}$.

3.3 Analysis Method

There are many methods that can be employed to characterize the degree of coacervation. Each of them gives specific insight of the system that we want to know about. In this research, the degree of coacervation is measured by the surface area, radius of gyration (R_g), radial distribution function (RDF), and mean squared displacement (MSD).

One method to calculate surface area was carried out in OVITO. In the work done by Song and Mendelev[74], surface mesh was utilized to measure the BCC structure, the least stable structure, in terbium phase competition. With this method, a phase transformation from BCC to HCP, a more stable phase, was well-identifiable. The work carried out by Melchor et al.[75] also utilized surface mesh to measure the model of layered silicon porous in the carbon infiltration process. They managed to identify layered porous silicon that is composed of porous silicon matrix (PSm) which has different porousities; in turn, their model of porous silicon confirms the actual experiment. In terms of porousity, the surface mesh also assisted the work done by Deluigi et al.[76] to measure porousity of the nanoporous high-entropy alloy in a simulation of tensile deformation. With its proven reliability to measure less structured atom configuration, this method is suitable to quantize coarcevation.

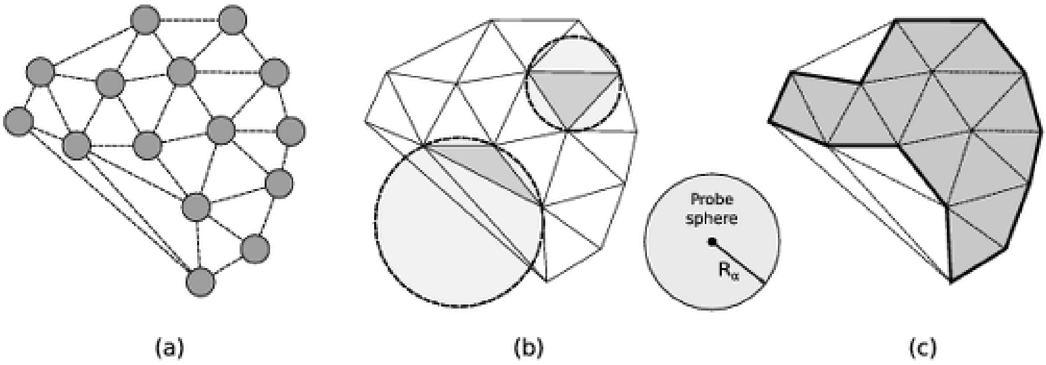

Figure 12: Schematic diagram of surface mesh measurement based on Delauney tessalation, adapted figure from reference [77] (a) Each beads construct triangular facets that will be evaluated. Evaluation of the region where a probe sphere is introduced(b). If the triangular facet is smaller than the probe sphere, it will be determined as filled region, otherwise it will be determined as empty region (c)

The OVITO's surface area employs the Alpha-shaped method that works based on the Delauney tessellation[77]. The beads act as points where 3 closest beads construct a triangular facet. A sphere radius (R_a) is introduced to evaluate constructed triangular facet. If a facet constructs a sphere that is smaller than R_a, it will be determined as filled region. If the facet's sphere radius is bigger, it will be determined as empty region.

Since the resulting surface still reflects atomic step that typically present on the surface of atomic object, an overestimation of the macroscopic surface might occur. Therefore, an fairing procedure[78] might be needed to obtain a smooth result.

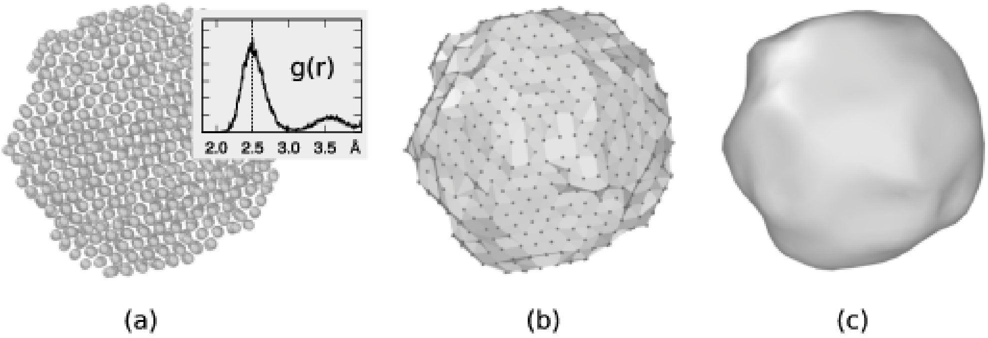

Figure 13: (a) Atomistic carbon nanoparticle with corresponding distribution function that its first peak distance is utilized as R_a (b) Constructed surface mesh after probe sphere evaluation (c) Final result after six iterations

It should be noted that the surface mesh highly depends on R_a. Big R_a will result to rough surface constructed, whereas R_a that is smaller than half of typical interatomic distance will create artificial voids. However, OVITO will automatically show the typical closest interatomic distance before calculating the surface.

Besides OVITO, surface area can also be measured by the Solvent Accessible Surface Area (SASA) performed on Visual Molcular Dynamics (VMD). The principal work of this method is pretty similar like OVITO's Alpha-shaped method, yet Delauney tesselation is not constructed. A sphere with a certain radius is introduced in the system to evaluate the surface area of each bead that can get in contact with the probing sphere.

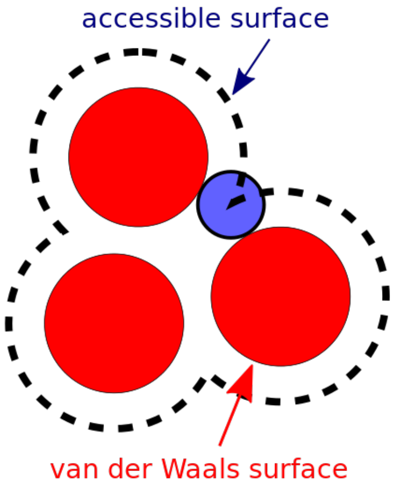

Figure 14: Blue sphere acts as probing sphere to evaluate the accessable area of red beads. Accessible surface can be indicated by the trajectory (dashed line) of the probing sphere

Large radius of probing sphere will result to a minimum accessible surface area since the sphere does not penetrate enough into the group of atom. Meanwhile, small radius will evaluate the surface area of the whole beads and result to unclear shape of the atom group. The typical radius is 1.4 which approximates the radius of water molecule, as the solvent. In this research, the radius was set to 1.6. A theoretical calculation was also being done with a consideration of a condition where all the beads are completely separated. The N beads in the system will indicate a maximum value of the surface of $N4\pi r_{beads}^2$.

The Radius of Gyration (R_g), characterize the size and conformation of the PE in the coacervate. It is defined by the root square of the average value of the distance that separates each bead with the center of the mass of the chain.

$$R_g^2 \equiv \frac{1}{N}\sum_{i=1}^{N}\left(\vec{R_i} - \vec{R_{cm}}\right)^2 \tag{21}$$

The R_g of PE coacervate was obtained by averaging the R_g of every single chain of PE.

Mean Square Displacement (MSD) describes the position evolution of the atoms in the system during simulation. In this system, it is useful in giving information how PE chains evolve during the simulation until coacervation occurs. The calculation of MSD is based on Freud's method [79]

$$MSD(m) = \frac{1}{Nparticles}\sum_{i=1}^{Nparticles}\frac{1}{N-m}\sum_{k=0}^{N-m-1}\left(\vec{r_i}(k+m) - \vec{r_i}(k)\right)^2 \tag{22}$$

where $r_i(t)$ defines the position of particle i in frame t. According to equation 22, MSD represents the average displacement calculated across the windows of length m throughout the simulation. Hence, for each m, $MSD(m)$ is calculated as the average over all windows of length m and over all particles.

Radial Distribution Function (RDF) describes the density of surrounding atoms in a certain radius. In a polymer network, especially in the term of coacervation, it provides information about the conformation and structure of the network. The RDF was calculated via mdanalysis which works on based on equation[80], [81]

$$g_{ab}(r) = (N_a N_b)^{-1}\sum_{i=1}^{N_a}\sum_{j=1}^{N_b}\langle\delta(|\mathbf{r}_i - \mathbf{r}_j| - r)\rangle \tag{23}$$

4 Results and Discussion

To have a better understanding of how the architecture of the networks affects the behavior in the DN system, the "Result and Discussion" section contains three sequentially ordered parts, Network Scale, Polymer Chain Scale, and Tensile Test. The network scale analysis will provide insights into the system regarding coacervation as a polymer network. Here, the phase separation between first and second was measured by OVITO surface mesh and VMD SASA calculation. Besides give numerical value, OVITO surface mesh also give graphical visualization hence the behaviour of the system during simulation could be well observed. The polymer chain scale analysis provides further details about what happened in the system from the point of view of polymer as a chain, which, in turn they affect the structure of the network. Average of radius of gyration will be discussed to illustrate the extent of a single PE chain's extension. Mean Squared Displacement provides insights about the covered evolution distance of PE beads in the equilibration the DN system was created. Radial Distribution Function describes the number of neighboring atoms surrounding PE beads.

4.1 Network Scale

4.1.1 OVITO surface mesh

Besides visualization, coacervation is also nicely quantized by OVITO's surface mesh[82] method. In general, OVITO's surface mesh provides a tool that supports modeling a relatively random configuration of atoms. As is well-known, solid elements tend to configure in periodic crystalline structures such as FCC, BCC, HCP, etc. These structures can be identified well by template matching. The characteristic properties can also be calculated analytically since correlated formulas are provided. Meanwhile, some less dense elements have no fixed configurations. To model the structure of atoms in a random configuration, surface mesh method can provide an alternative solution.

The surface mesh will identify any evolution of the DN structure during equilibration. As a natural behavior of oppositely charged compounds to aggregate, the collapsed PE will form a cluster. The formation of the cluster contains beads that suits surface mesh method scheme thus its structure can be measured.

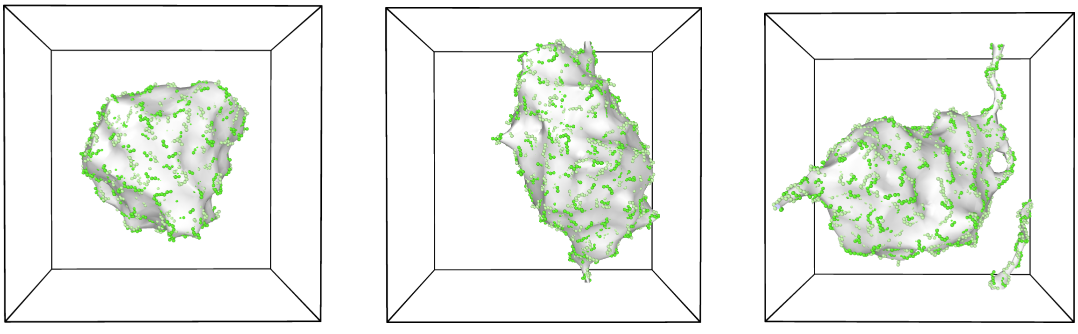
(a) (b) (c)

Figure 15: Snapshot of constructed surface mesh of PE. All have the total same number of beads of PE. The blob constructed based on the structure of the DN. By the value, the surface are increase from (a) to (c). These snapshots only show PE without neutral polymer network.

The OVITO surface mesh visualization of PE complexation is designed to resemble the structure of the coacervate in actual experiments. When a DN undergo a phase separation, a dense and supernatant phase are formed. The cluster of PE represent the dense phase of the system, as it is visualized in Figure 15.

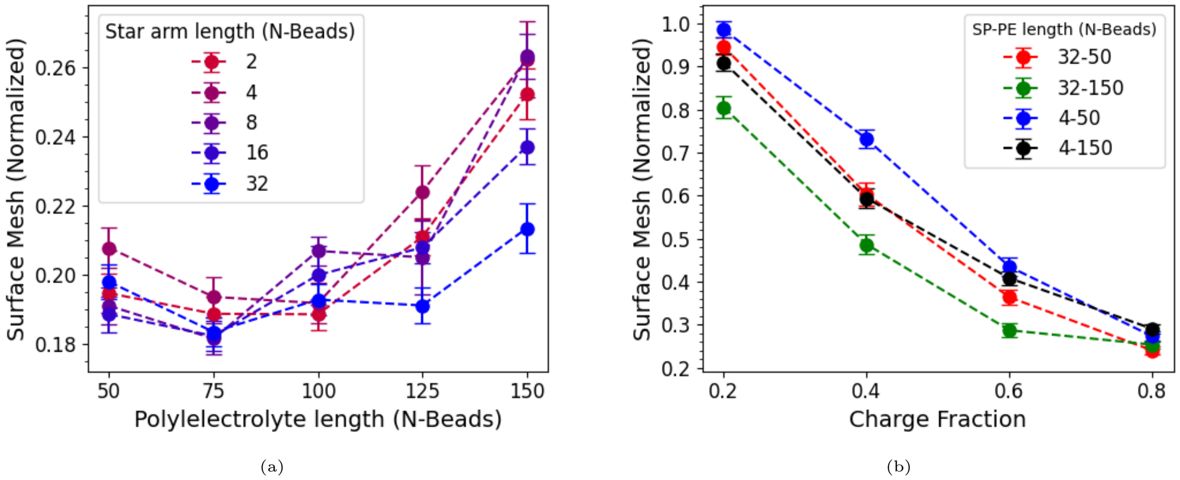

Figure 16: Normalized surface mesh value of system in different length of PE and different length of star polymer (a). Despite the trend not being smooth, shorter PEs tend to have smaller surface values compared to longer PEs, indicating that shorter PEs are more phase-separated than longer PEs. However, the effect of star polymer length is less pronounced. Chosen systems resembling the longest and shortest chains with high and low crosslink density are simulated at different charge densities of PE chains (b). All systems exhibit a similar trend of decreasing surface mesh values as the charge density increases, indicating that charge density promotes coacervation.

Longest PE tend to show relatively higher value of surface. A non-smooth increasing trend is shown from shortest to longest PE. In terms of Star arm length, the trends are seem unclear. However, the 32 beads Star arm length relatively tend to have lower value compared to others. Different architecture of the networks lead to different value of constructed surface, As it is shown in Figure 16a. Here, the surface mesh values are normalized as a fraction of the maximum value. The maximum value was obtained by averaging the surface mesh from three simulations with 50, 100, and 150 PE beads, keeping the total number of 12000.

The behavior of PE complex coacervation, in terms of their length, can be viewed in many aspects. From the counterion condensation perspective, short chains experience stronger counterion condensation, leading to a lower effective charge and reduced electrostatic repulsion, which in turn decreases chain stretching and promotes PE aggregation[83]. The reduced electrostatic repulsion in short chain is also caused by stronger charge screening since their effective charge is neutralized more by surrounding counterions[84]. As a result, electrostatic repulsion is weaker, and the polymer adopts a more collapsed conformation. Since the charge of PE chains play big role in the complex coacervation, the effect of charge density on PE chains was also investigated as shown on Figure 16b. In the systems of different PE chains and different crosslink density of neutral network, all systems exhibit similar trend of decreasing surface mesh value at high charge density, indicating a high degree of coacervation is achieved. However, it should be emphasized that the objective of this work is not to achieve a high degree of coacervation, which would indicate that the networks are completely separated, but rather to understand how the architecture of both networks and the charge density of PE chains promote interpenetrating network formation, as this is the expected structure of DN hydrogels.

Ideally, the movement of PE is influenced by the structure of the star polymer (SP).

Regarding crosslinking density, longer star polymer arms correspond to lower crosslinking density, and vice versa. Lower crosslinking density provides more space for PE to move, making aggregation easier. Besides crosslinking density, The conformation of SP network also affects the formation of PE clusters. In the same structural architecture, three different replica of systems were generated by varying the random velocity in the LAMMPS. While these structures may have the same crosslink density, their formation can still differs.

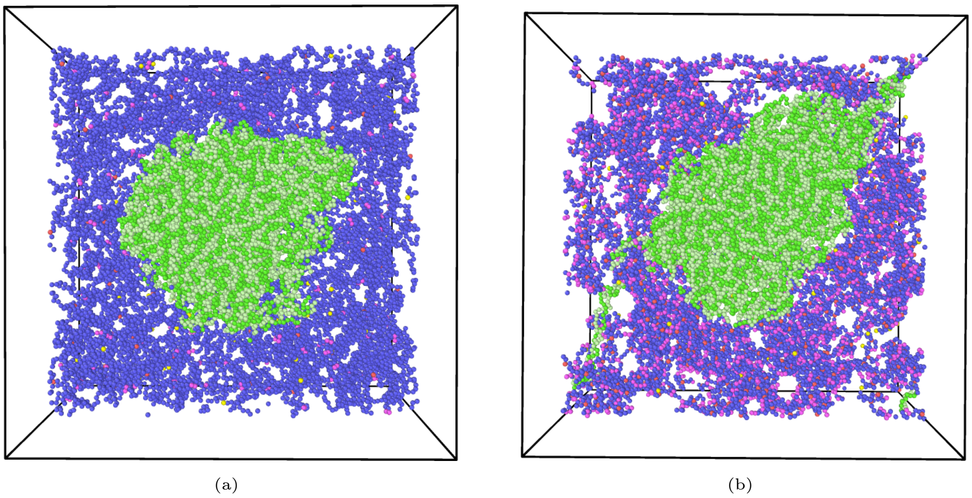
(a) (b)

Figure 17: sliced snapshot of two different systems. (a) 32-50 (Star Polymer - PE) has lowest crosslinking density, allowing PE to freely move. (b) 4-150 has high crosslinking density indicated by purple beads.

The initial position of PE is mainly affected by the process of creating network in crosslink simulation. When crosslink of the SP is created, the PE could be tangled with the SP, hence its following movement in the desalting process is limited. Nevertheless, the entanglement does not significantly occur. If we have a look on Figure 17, rather than create entanglement inside PE blobs, the crosslink of SP limits the movement of PE outside the blob instead. Therefore, the effect of crosslink density is less pronounced.

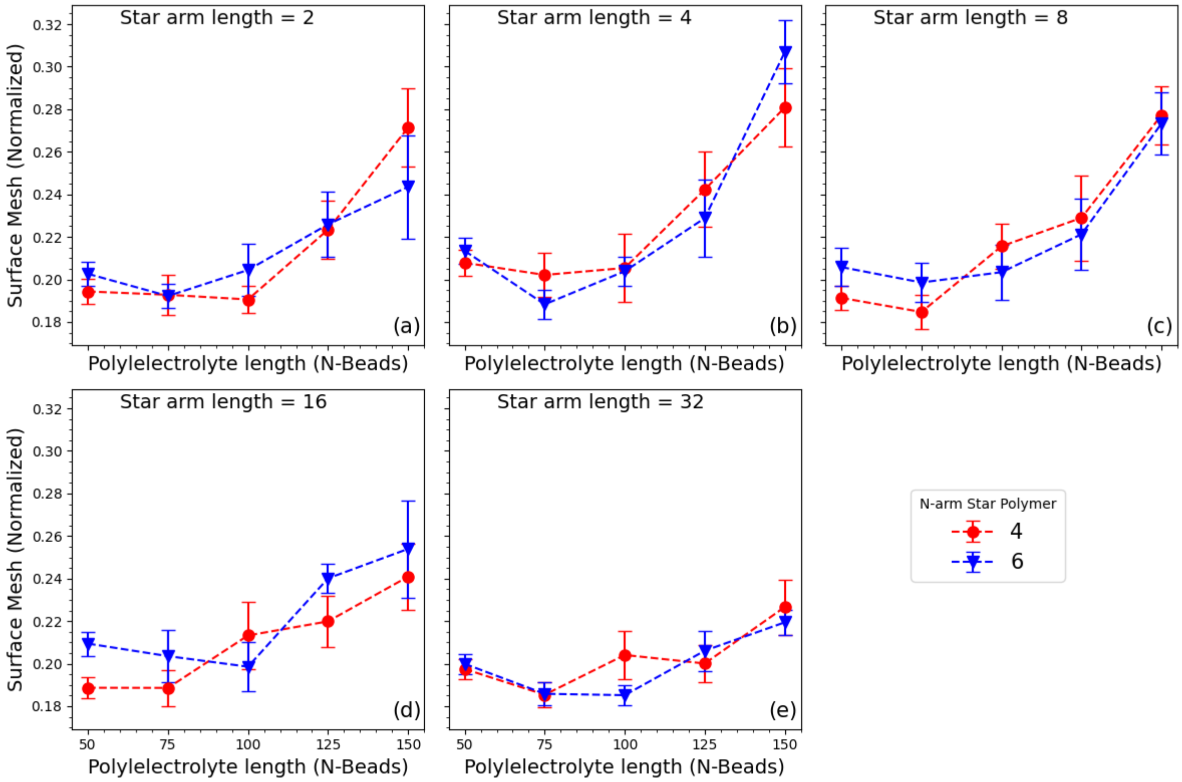

Figure 18: The surface mesh compares the 4-arm and 6-arm star polymers. The 6-arm polymer indicates a higher crosslink density in the neutral network. Increasing crosslink density is expected to enhance the formation of an interpenetrating network during the coacervation. However, the effect of crosslink density on coacervation is less pronounced.

The effect of crosslink density is also displayed in Figure 18 which shows the comparison between 4 and 6 arms of the SP. The 6 arms SP indicates the higher density of crosslink shows no significant difference of surface compared to 4 arms SP.

However, it should be noted that the noises of error occur due to each system has different time to achieve equilibrium state. At equilibrium, the system achieves a stable phase structure as a result of the balance among attractive electrostatic interactions, counterion entropy, and solvation effects[85]. Within the same time of equilibration after desalting process, some systems have a constant surface of PE over time, whereas PE in other systems still show an intention to aggregate more as is shown in Figure 19. Especially for the long chains with 125 and 150 beads, the plot still plateaus.

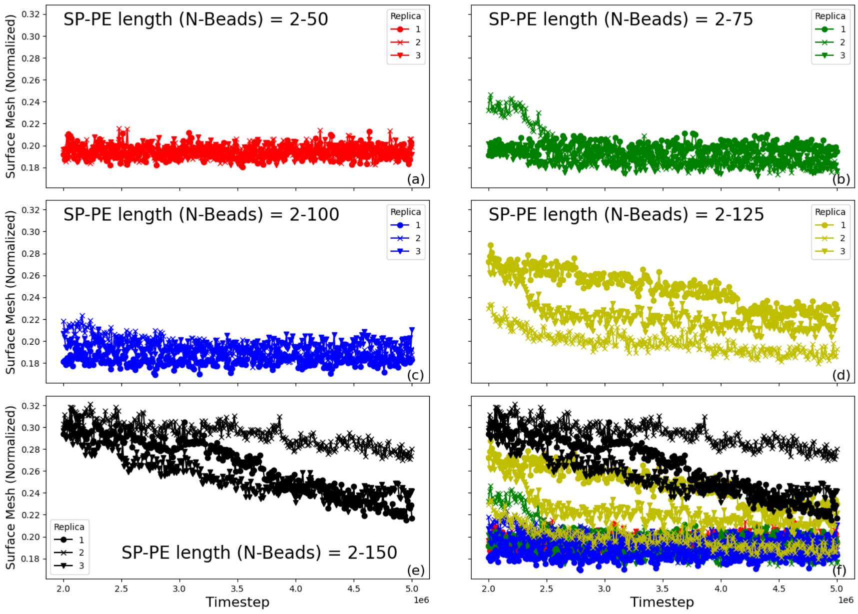

Figure 19: The plot of surface mesh versus timestep represents the equilibrating behavior of the system with different-length PE chains. Each chain system has three different replicas. The equilibrium state has been achieved for the shortest PE chain (50 beads) since the surface value remains constant over the timesteps. However, for chains with lengths of 125 (d) and 150 (e) beads, the plot still plateaus, indicating that the system continues to aggregate during phase separation and has not yet reached equilibrium.

In a short time simulation, long-range electrostatic interactions and counterion dynamics might not be fully accounted[86]. The ongoing aggregation indicates that the PE chains are still dynamically evolving, which suggests that the system is still finding a lower free energy state[87]. Hence, the system is not yet equilibrated. An ideal comparison should be taken from all equilibrium states. However, based on this work, equilibrium has not been achieved even after 5×10^6 timestep. Therefore to achieve equilibrium, simulating equilibration with timestep beyond 5×10^6 is recommended.

4.1.2 VMD Solvent Accessible Surface Area

The Solvent-Accessible Surface Area (SASA) was firstly introduced by Lee and Richards[88] to investigate the topology of the surface of a protein. The topoloy is closely connected to its function of the interface between solvent and a partial part of the protein surface, resulting in the structure of the native molecule; and the chemical reactivity that highly depends on this interface. In the work done by Ma et al.[89] investigating mechanistic of membrane fouling in organic solvents, SASA managed to measure the adsorption rate of a dextran in different solvents, illustrating the interaction between dextran, membrane, and solvents. Chen and Panagiotopoulos[90] in their work utilized SASA to measure surface tension associated with hydrophobic interactions in surfactant micellization. Generally, the SASA provide a powerful method to measure constructed structure of compounds as well as their interaction with solvents. Nevertheless, this work has limitation of SASA only for measuring the constructed structure of PE. Noting that SASA works based on Van der Waals radius, a theoretical calculation of condition where the beads are completly separated, indicating the highest value of SASA, can be obtained, a feature that can not be done in OVITO surface mesh.

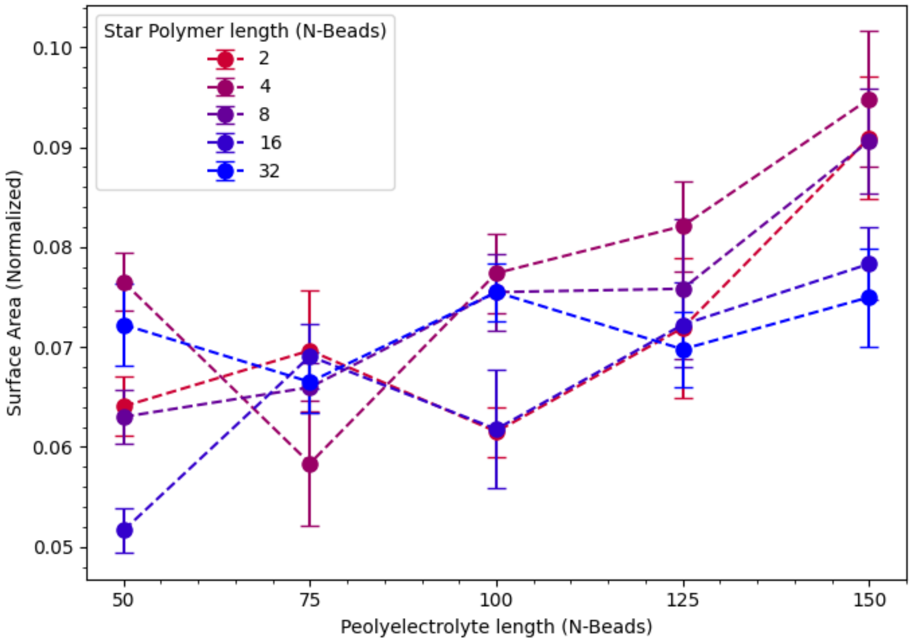

Figure 20: The normalized SASA value of the system for different PE lengths and different star polymer lengths. Similar to the OVITO surface mesh, although the trends are not smooth, an increasing trend is observed as the PE length increases.

A similar trend like the OVITO surface mesh is shown in the figure 20. An increasing trend along increasing length of PE is shown, whereas the trend in increasing the length of star arms seems not obvious. The value of surface area is normalized by a fraction of maximum value that is obtained by $A \approx 4\pi r_s^2 \times N_{particle}$ where $r_s = 1.3\sigma$ and $N = 12000$. Since this work is based on coarse-grained simulation, the effects of solvent are approximated since the solvent is treated as a continuum that interacts with the solute through a dielectric constant and a few other parameters. Hence, further analysis is required to investigate the effect.

4.2 Polymer Chain Scale

4.2.1 Radius of Gyration

The Radius of Gyration (R_g) is defined as the average radius that calculated from the squared distance of each monomer to the center of the mass of the polymer [38]. The R_g gives a clearer measurement of a polymer in a random conformation. Two polymers might have the same number of monomer, yet if one is more stretched and the other is more crumpled, R_g would be different. Many aspects might influence the conformation of the polymer, thus it affects R_g as well. Accroding to Nierlich et al.[91] in a charged system, the local flexibility of the polyelectrolyte will be affected by electrostatic repulsions, hence the global size of polyelectrolyte will tend to increase. Hsiao and Luitjen[92] showed in their work that the collapse and extension of R_g of the polyelectrolyte can be controlled by multivalent-monovalent salt concentration. In this work, R_g of each chain is measured when the PE networks are completely constructed, at the equilibration after desalting process finished.

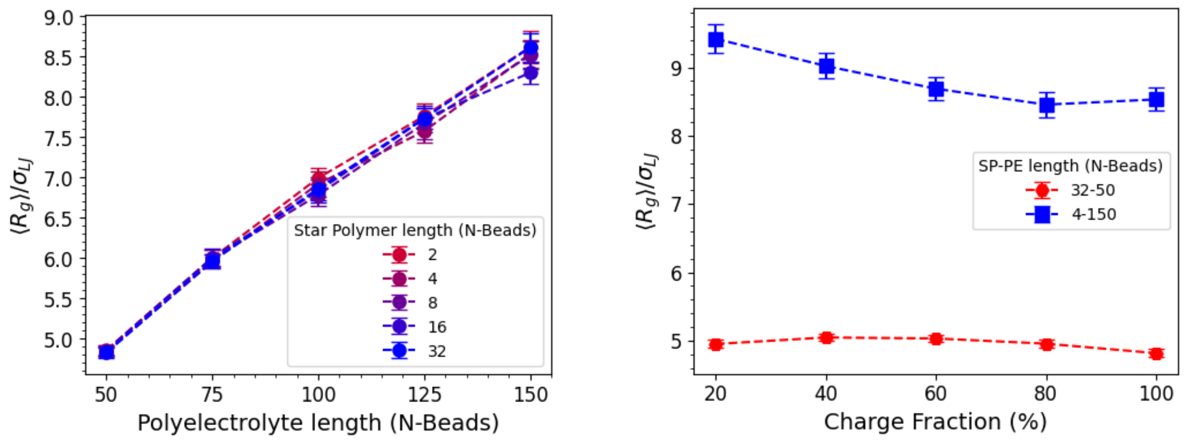

(a)

(b)

Figure 21: Colored dots in gradation style represent the R_g of PE in different length, agree that the R_g is increasing as the length of polymer increases as well. Radius of Gyration in different charge fractions (a). The charge was varied in 20% to 80% with increment 20% (b). Ideally, a lower charge fraction reduces electrostatic interactions, leading to less complexation. However, this effect is more pronounced in the longest PE chains.

Based on the theoretical calculation showed by Rubinstein [38], R_g of ideal chain can be determined by the equation

$$\langle R_g^2 \rangle = \frac{b^2}{2N^2}\frac{N^3}{3} = \frac{Nb^2}{6} \tag{24}$$

where N is the number of monomers and b is associated to Kuhn length. Equation 24 obviously shows that longer PEs tend to have higher Rg as is confirmed in Figure 21a. However, the calculation of R_g of ideal linear chain neglects interaction between monomers that are far apart along the chains. Meanwhile, in the performed simulation the FENE and harmonic potential is utilized, where their presence introduce bond stiffness that limits the flexibility of the chain. Therefore, the R_g values are higher than the theory.

To gain a better understanding on how electrostatic interactions influence the conformation of PE, the charge fraction was varied in two samples of longest PE - highest crosslink density and shorter PE - lowest crosslink density, shown in Figure 21b. A clearer difference is observed in the 150-mer system. The higher charge fraction leads to a more collapsed conformation of PE, and hence, R_g decreases as well. Nevertheless, the effect is not so apparent in 50-mer system, as shown by less smooth trend. Interestingly, the decline trend from the 80% to the full charged fraction is more clearly observed in the length of 50 beads than 150 beads. On the other hand, the trend of from the 20% to the charge fraction of 40% is more clear in the length of 150-mer than 50-mer system. However, by observing from the error bars, the effect of charge fraction is more obvious in the long PE chains. The disparity between two samples might be caused by several factors such as inter-chain electrostatic interaction[93], chain length and correlation effect[94], and role of chain ends[95]. Stronger inter-chain electrostatic interactions are shown in longer PE chains due to contiguous charge along the chains, therefore, it forms more stable and compact complexes[93]. In the same total number of PE beads, shorter PE will have larger number of chain ends which might disrupt charge correlation[94], thus it leads to irregular trend of R_g, since individual chains might form smaller and less coordinated complexes[95].

4.2.2 Mean Squared Displacement

If R_g provides insights on the complexation of PE from the point of view of a single chain, the mean squared displacement (MSD) would provide information about the evolution of mobility of each beads of the PE chains. In the work done by Yulia et al.[96], MSD managed to describe the mobility of counterions in a system with a high electrostatic strengths, and revealed that the counterions of strong PE, indicated by a higher ratio size between counterion and monomer, tend to move freely along the chain. In this work, MSD was utilized to gain insight on the formation of PE in different architectures of networks. Same like the measurement of R_g, The MSD was measured during the equilibration process after desalting process is done performed.

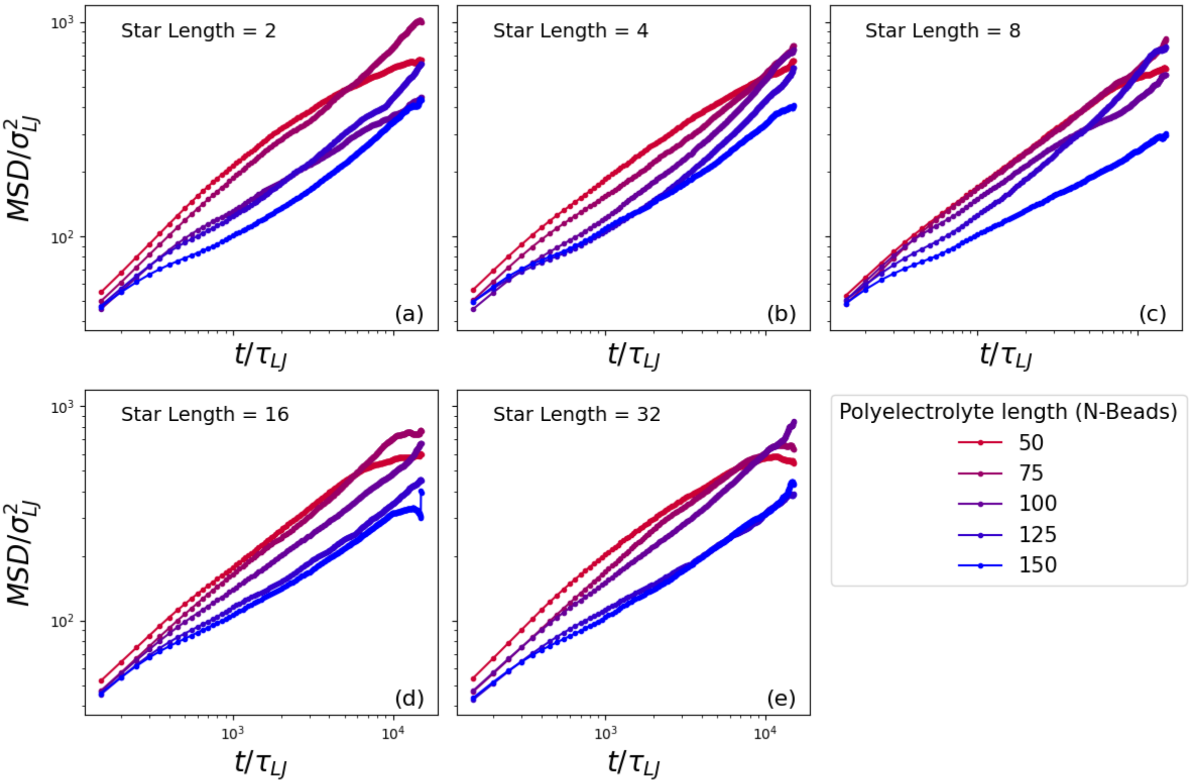

Figure 22: Mean Squared Displacement (MSD) of different PE length in the same star polymer (SP) length. The shortest PE chains (50 Beads) are represented by the red lines whereas the longest chains are represented by the blue lines. The figure (a) displays the systems of different PE length in the shortest length of SP, indicates the highest crosslink density, whereas figure (e) displays the systems in lowest crosslink density. In general, shortest PEs have highest mobility whereas lowest mobility belongs to longer PE. This trend is averagely similar in the different crosslink density.

In systems of the same length of SP, the shortest PE chains (50 beads) are likely to have the highest MSD, while the longest PE chains (150 beads) have the lowest MSD as shown in Figure 22, indicates that shorter PE are more free to move. This phenomenon is aligned with many factors. Since shorter polymers have greater flexibility compared to longer ones [38], therefore, shorter polymers have greater segmental motion than longer ones[97]. Looking from the external factor, in the presence of SP as the surrounding medium, the motion of shorter polymers is less restricted[98], support them to move more freely. In the same total number of beads, shorter PE have a higher proportion of chain ends, which generally are more mobile than interior segments and give a significant contribution to overall mobility and diffusion behavior of PE chains[99]. Longer PE chains also display stronger electrostatic interactions, thus they mobility are more restricted[100].

Additionally, it should also be noted that the counterion release influences the formation of polyelectrolyte chains by reducing electrostatic repulsion between charged sites, in a way extended formation of long PE chain and more collapse formation of short PE chains[96]. Therefore, this difference in formation also affects the mobility of PE chains.

The role of SP as the second network is also investigated, as shown in Figure 23. Note that this network is neutral and there is no electrostatic interaction with PE network. The fact that the proportion of SP and PE is high (70:30), leads to the domination of physical interactions in the system. Here, the SP network acts only as the medium that restricts the mobility of PE.

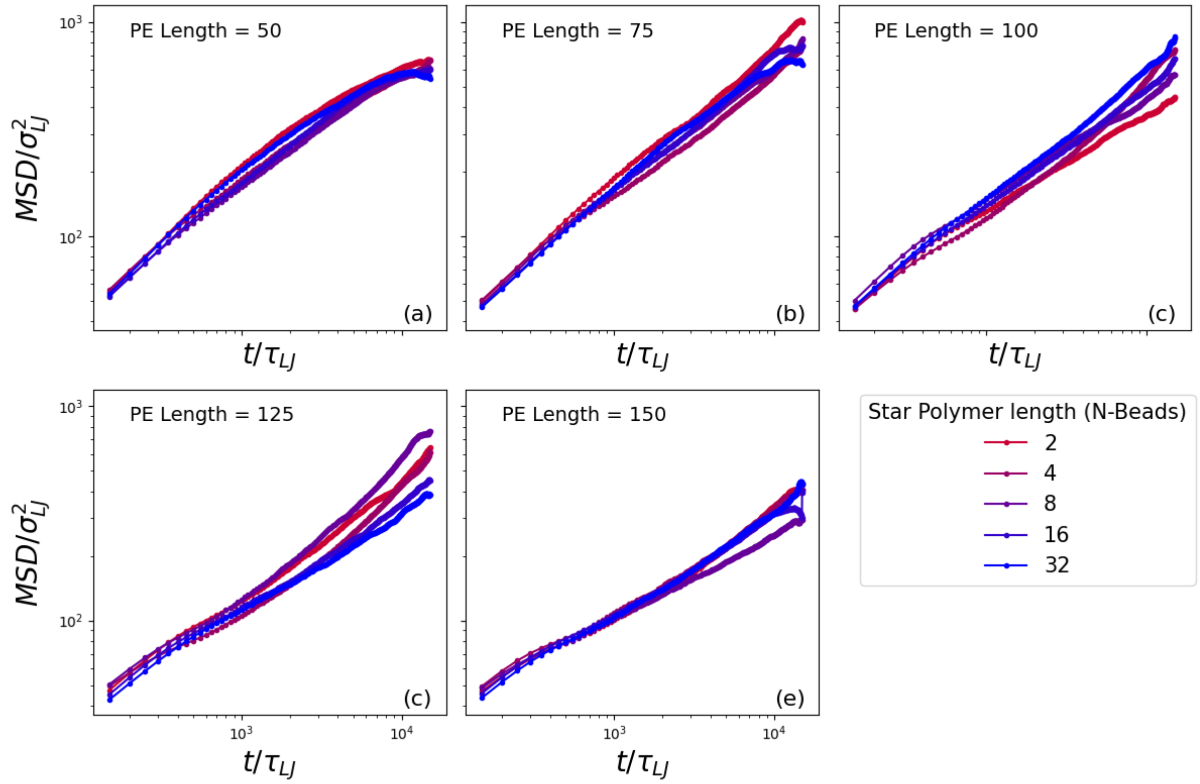

Figure 23: Mean Squared Displacement (MSD) of different SP length in the same PE length. The shortest SP length, indicates the highest crosslink density, is illustrated in red lines, whereas longest SP in blue lines. Within the same length of PE, the influence of the varied crosslink density is not much apparent, indicated by fairly similar trend of different crosslink density.

However, the varied length of SP, that indicates varied crosslink density, displays no significant effect on the motion of PE. The motions of a PE of certain length in the different crosslink densities are fairly similar. Despite this phenomenon, ideally, the high crosslink density will form a rigid and dense matrix, restricting the motion of charged PE. This effect was probed by Perez et al.[101] where they found out that the mobility of a polymer network is more restricted in a more rigid neighboring medium.

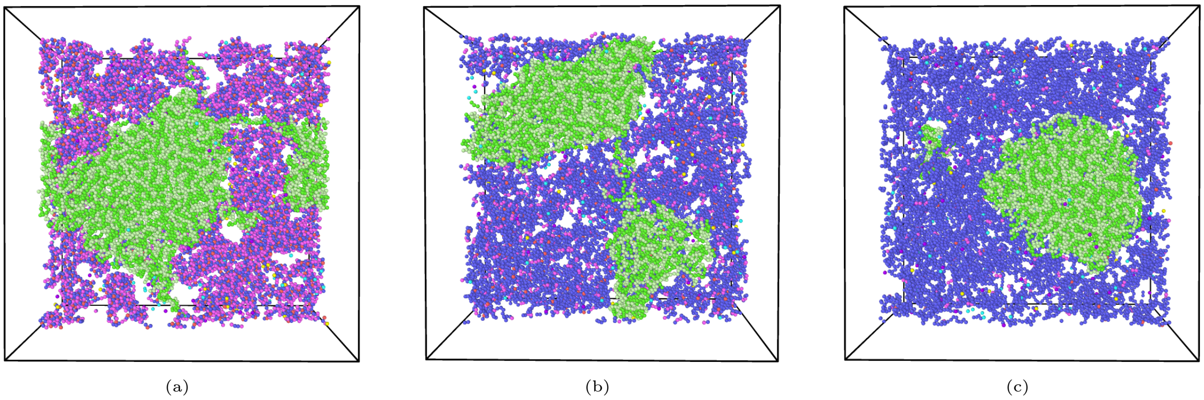
(a) (b) (c)

Figure 24: Half-sliced snapshots of the system of same PE length (150) in different SP length. Shortest SP length(a) indicates higher crosslink density. Crosslinks are shown by bright purple beads. Figure a, b, c, represent highest, middle, and lowest crosslink density respectively. The PE complexes in the high crosslink density is more separated whereas low crosslink density shows a more aggregated PE complexes

If we look at Figure 24, the highest crosslink density (a) forms PE complexes more separated. On the other hand, PE in the lowest crosslink density (c) already concentrated in a certain region. Thus, the separated part of PE in high crosslink density might have possibility to aggregate to the main part. However, such condition might require tremendous long time step of simulation. It should also be noted the fact that the longest SP chain is 32 beads, whereas the shortest PE chain 50 beads. Therefore, in the complexation after salt are completely removed, the possibility of PE to encounter each other is higher than the possibility of their motion being restricted by SP network.

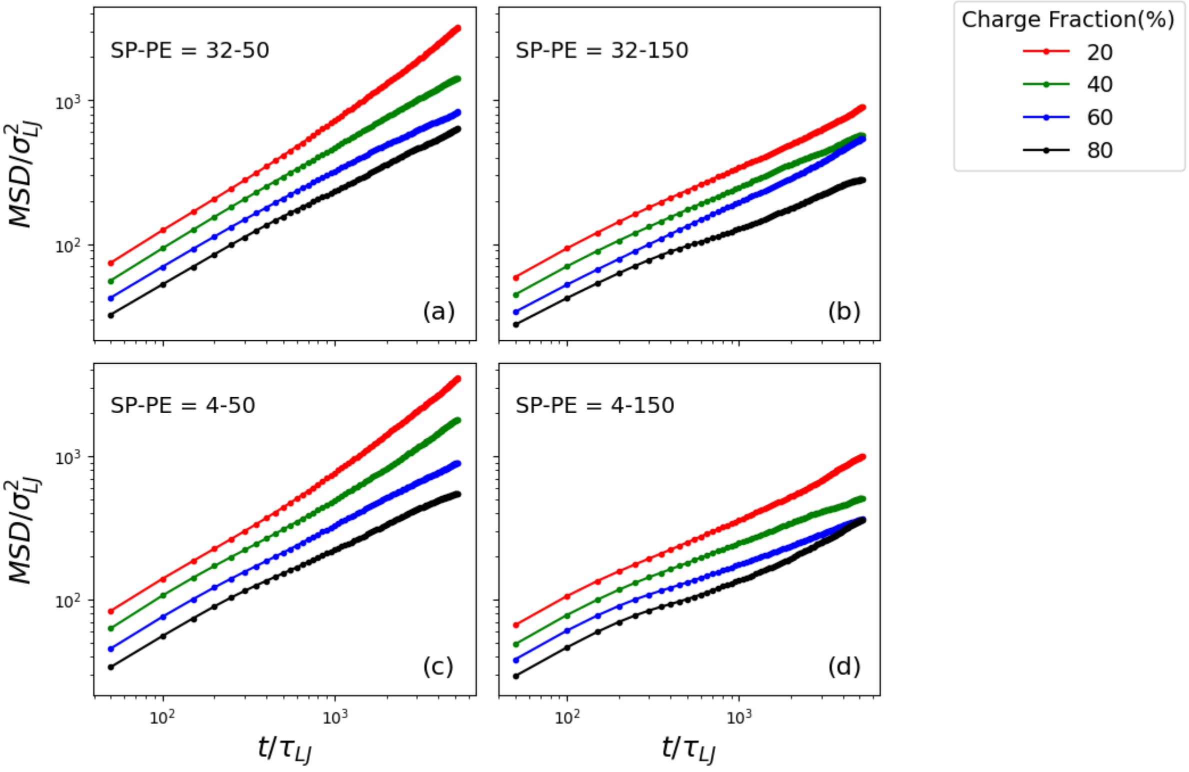

Figure 25: The MSD plot shows different charge densities of the PE chain in various systems. The two top figures represent the systems with the shortest PE (a) and longest PE (b) in a low crosslink density star polymer. Similarly, the two bottom figures correspond to the shortest PE (c) and longest PE (d) in a high crosslink density star polymer. All figures exhibit the same trend, where the lowest charge fraction shows the highest mobility, indicating that their motion is less restricted by electrostatic interactions

The MSD of the systems at different charge densities of the PE chain is displayed in Figure 25. The systems include the longest and shortest PE chains at the highest and lowest crosslink densities of the star polymer. All plots show the same trend for different charge fractions, with the lowest charge fraction having the highest MSD, indicating that mobility is less restricted due to weak electrostatic interactions. The trend in this plot further confirms that electrostatic interactions restrict the mobility of PE, just as they do in a fully charged system.

4.2.3 Radial Distribution Function

Since the mobility of PE is also influenced by SP as the surrounding media, the radial distributional function (RDF) can be a useful tool to quantify spatial organization and interactions in the DN system. The RDF describes the probability of finding particles at a certain radius from a reference particle relative to a uniform distribution. In the work done by Zhang et al.[102], RDF was utilized to describe the distribution of water molecules in the DN composed of agar and PAM networks. In a theoretical work, Zandi et al[103] show that RDF provides information about the structural formation of PE and worm-like chain (WLC) polymer. In terms of steric interactions in a DN system, RDF can provide insights on how PE and SP are spatially distributed and how steric effects affect their organization.

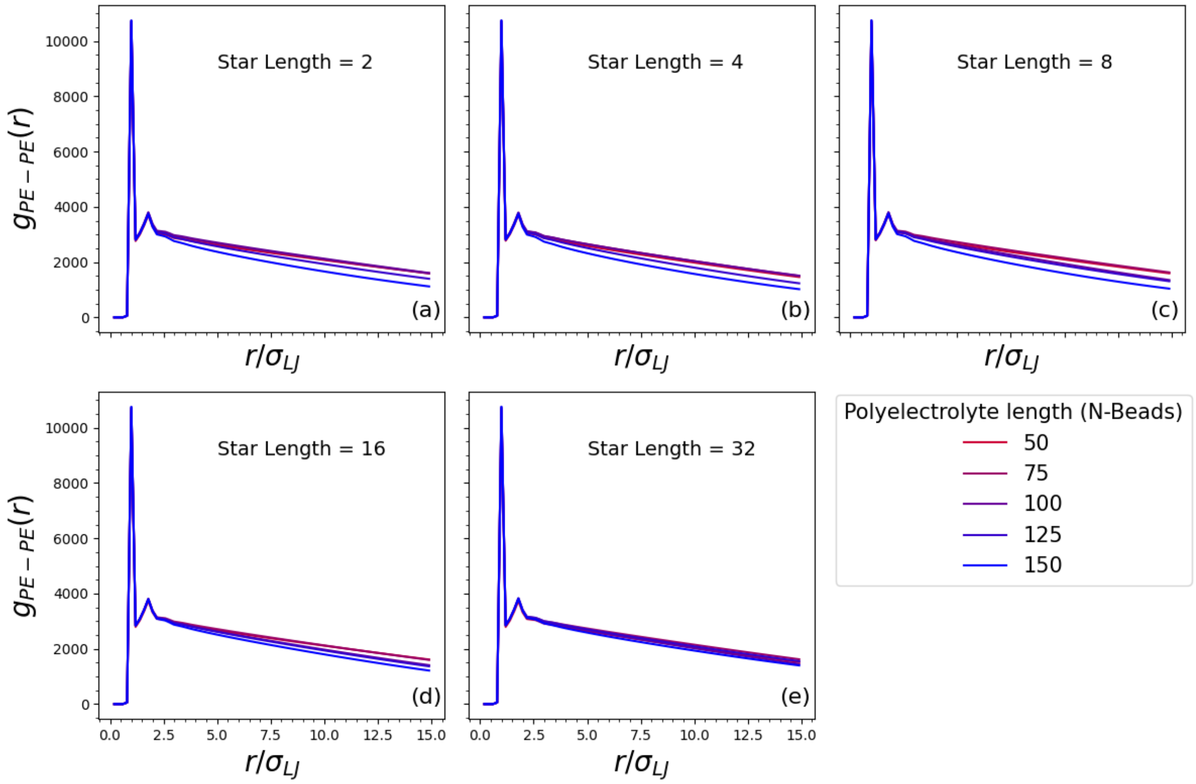

Figure 26: RDF of different length PE in the same crosslink density of SP. From (a) to (e), the length of SP increases, indicating the decline of crosslink density. In the same all crosslink densities, the longest PE tends to decline more steeply at the radius beyond 2.5, as the stronger electrostatic interaction that occurs in longer PE chain support local aggregation but restrict longer-range organization

Figure 26 show the RDF that encompasses the distance between polyelectrolytes. In the same crosslink density of SP, despite different lengths of PE have fairly similar trend, beyond $r/\sigma_{LJ} \approx 2.5$, longer PE tend to have steeper decline. Nevertheless, if we look at the radius where RDF shows highest peak ($r/\sigma_{LJ} \approx 0.995$), the longest PE chain has the highest peak, as shown in Figure 27.

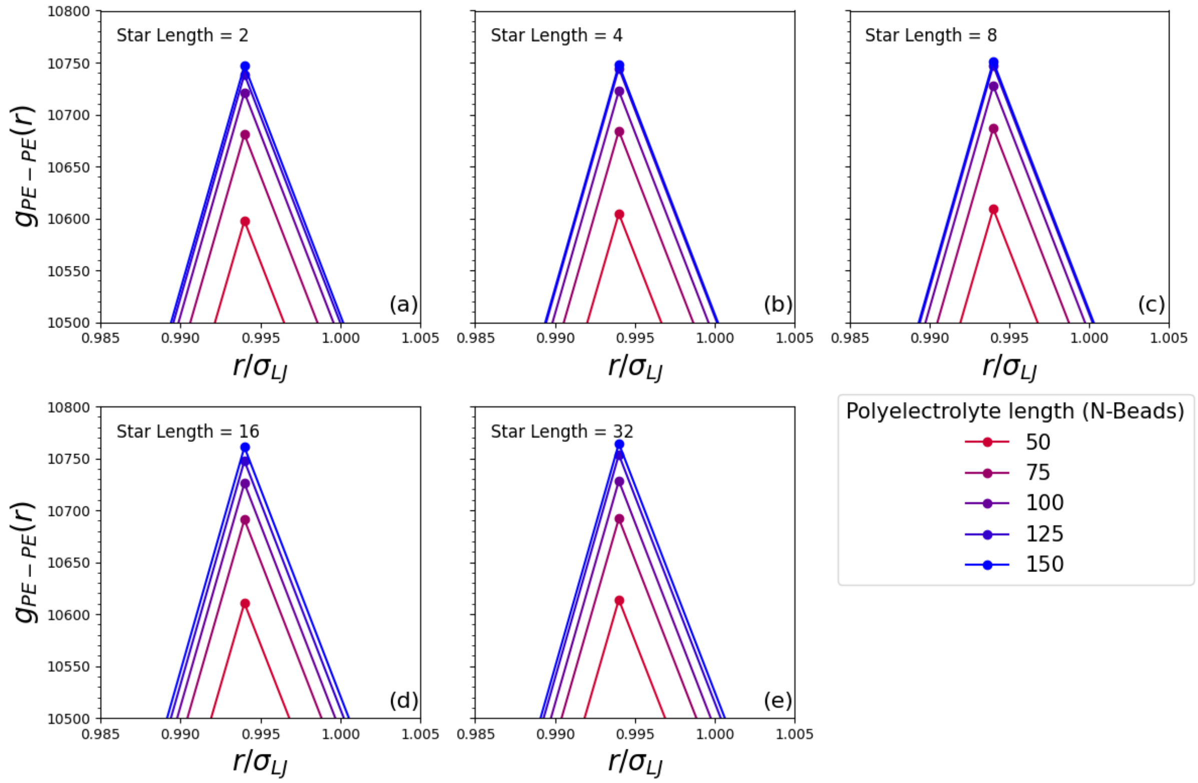

Figure 27: The peaks of RDF of each PE in the different crosslink densities. Highest density is displayed in figure (a) and lowest density in figure (e). All system agree that longest PE has the highest peak and shortest PE has lowest peak, indicating that longer PE has stronger electrostatic interaction at the shorter distance.

This can be understood as the result of electrostatic effects where longer PE chain will have stronger electrostatic interactions and vice versa[95]. High peak at shorter distance indicates that electrosatic interactions promote local aggregation, yet they limit longer-range organization, resulting in steeper decline of RDF[104]. By visualization analysis, as it is discussed in the OVITO surface mesh, shorter PE tend to form complexation more aggregated, shown in Figure 28. The longest PE chains that collapse twistingly along their chain length aggregate in two regions, and are connected by a small fraction of PE. This small fraction also contribute to the steeper decline of RDF, since it is less surrounded by the same PE chains.

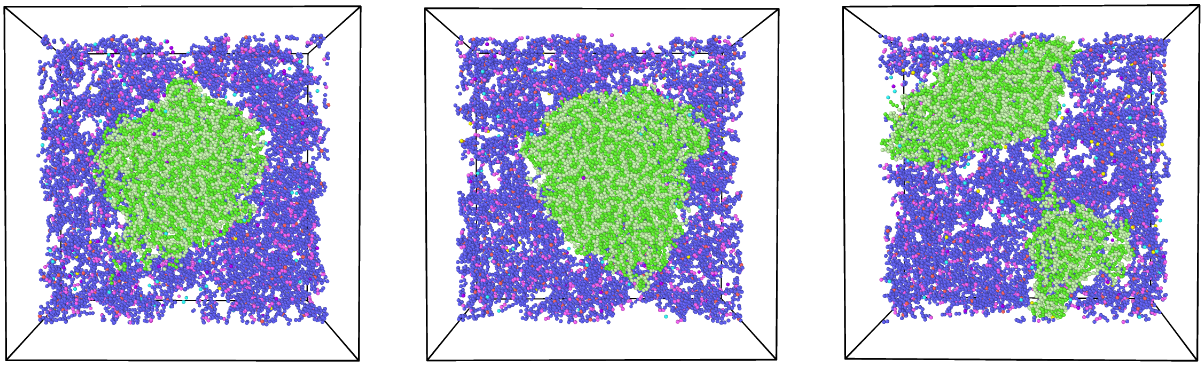

(a) (b) (c)

Figure 28: Half-sliced snapshot of the system of different PE length in the same crosslink density. The PE with length 50 beads (a) collapse more aggregated the PE with length 100 (b) and 150 beads (c). The longest PE aggregate twistingly in two regions that are connected by a small fraction of PE.

Meanwhile, shorter PE with weaker electrostatic interactions, rather than promoting local aggregation, allowing a more uniform distribution instead, leads to a slower decline of RDF. In the context of size, longer PE experience gretaer steric hindrance within SP network as a confining medium[105], leads to more restricted ability to move into larger distance.

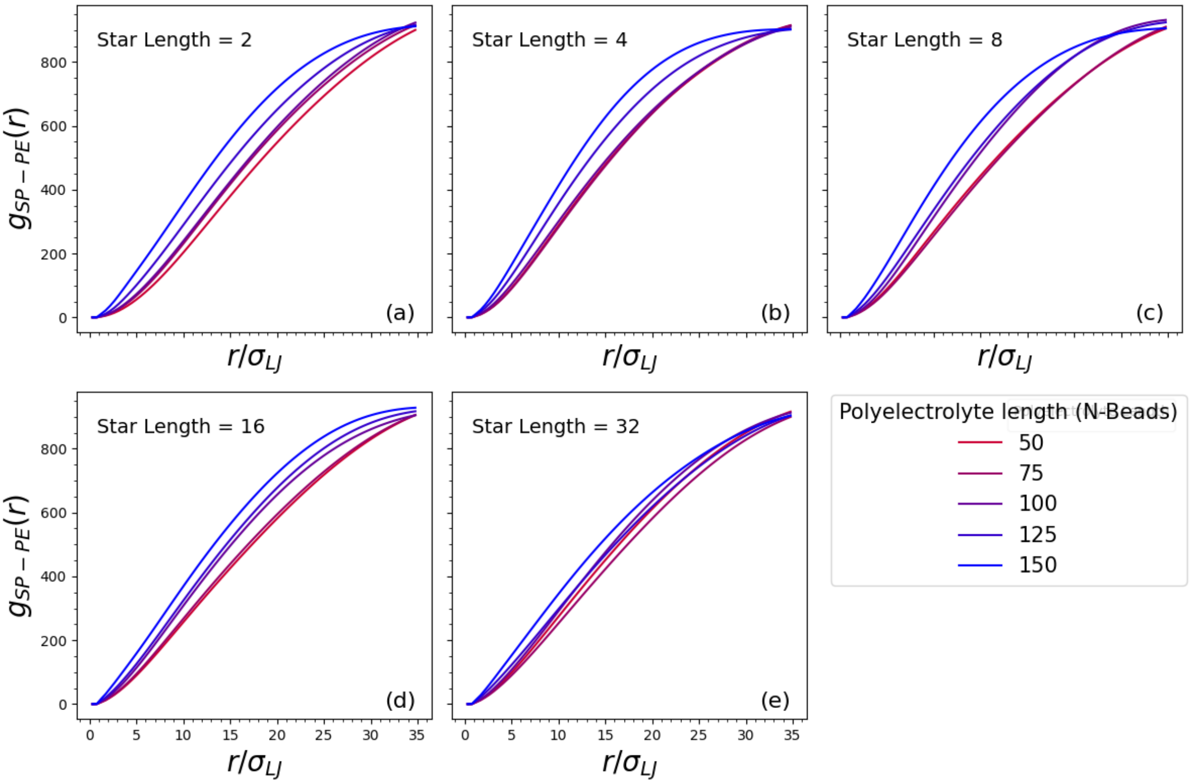

Figure 29: The RDF that covers the distance between PE and SP of different PE length in the same crosslink density. System with highest crosslink density is displayed on figure (a) and the lowest density is displayed on figure (e). All different density systems agree that the longest PE chain has the highest RDF, indicating that their configuration have closest distance to SP network. The continuous increasing trend of all system is due to the fact that the high proportion of SP in the DN system.

The RDF that encompass the distance of PE-SP were also investigated as shown in figure 29. Since the length of box size is 74, the maximum probing distance of RDF was set to

35. At the maximum distance of 35, RDF shows continuously increasing trends. This is a result of the high proportion of SP and the fact that SPs are distributed uniformly around the simulation box[106].

It can also be seen in the figure that the longest PE chain tends to have higher RDF. This indicates that the longest PE has the closest distance to the SP configuration, since they aggregate twistingly along the chain so they have higher possibility of entangling with SP compared to the shorter chains. This is a confirmation of the discussion in the network scale analysis section.

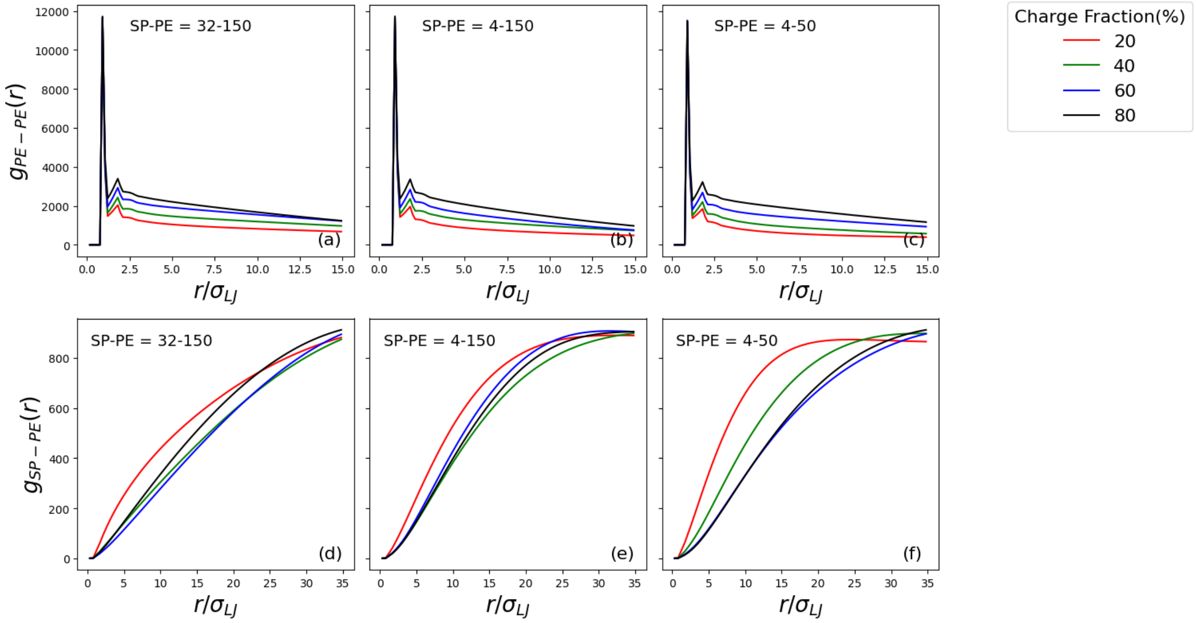

Figure 30: The effect of charge density in PE chains across different systems is analyzed. The top figures (a, b, and c) show the RDF plot of the distance between PEs, whereas the bottom figures (d, e, and f) represent the distance between PE and SP. While the top figures exhibit a similar trend, the bottom figures reveal that differences in the structure of the composing network in the DN system result in varied RDF values due to the mobility of PE chains during complexation.

The effect of the charge density on PE chains is displayed on Figure 30. Three systems were created based on SP-PE length, including: (i) 32-150, (ii) 4-150, and (iii) 4-50. The comparison between (i) and (ii) provides insight into how PE chains with different charge densities form in the highest and lowest crosslink densities of SP. Meanwhile, the comparison between (ii) and (iii) offers insight into how the longest and shortest PE chains with different charge densities form in the same crosslink density of SP.

The RDF plots of the distance to each PE confirm that the highest charge density of 80% exhibits the highest RDF value at the second peak. This indicates strong electrostatic interactions that maintain complexation. In the RDF plots of the distance between PE and SP, the lowest charge fractions dominate the high RDF values, indicating that PE with low charge density tends to associate with the SP network. However, in the comparison of the same PE chains at different crosslink densities, PE chains in the highest crosslink density exhibit a higher RDF value at short range, indicating they have more interaction with the SP network. Meanwhile, within the same crosslink density of SP, the lowest charge density of the shortest PE chains exhibits a higher RDF value, indicating more interactions with the SP network. This aligns with the MSD plot, which suggests that short PE chains experience fewer restrictions in their mobility. The effect of low charge density further enhances their mobility throughout the network.

4.3 Tensile Test

The effect of the double-network configuration on mechanical properties was investigated by performing a tensile test simulation. However, it should be taken into consideration that the structure of PE in the DN, rather than forming a percolating network, takes the form of a collapsed structure. Notably, with the SP:PE proportion being 70:30, applying uniform stress distribution along certain axis in some cases will cause the PE network to detach from the main network. It should also be noted that the applied strain rate is $0.001\varepsilon/10000$ timestep$_{LJ}$. Converting this rate to the real-time results in strain rate $\dot{\varepsilon} = 10^8 s^{-1}$. This is an extremely high value compared to experimental strain rates[107] such as quasi static testing (10^{-5} to $10^{-3} s^{-1}$), dynamic testing (10^2 to $10^4 s^{-1}$), and shock or impact loading (10^5 to $10^7 s^{-1}$). As a result, the tensile test outcomes are primarily influenced by the elasticity of the neutral network, while the role of the PE network is less pronounced.

Ideally, in performing a simulation of tensile test in the double networks system, a relaxation time should be taken to consideration. A work done by Drozdov and Christiansen [108] found that the DN gels featured with dynamic bonds display specific behavior of stress-relaxation under multi-cycle deformations, pointing out the crucial role of relaxation time in investigating material properties. Continuous strain will not allow networks to redistribute stress and return to an equilibrium state, leading to unrealistic results. Despite the tensile test simulations in this work were done continuously due to limited time and resources, hopefully it can give an insight about the effect of the network from an architectural point of view.

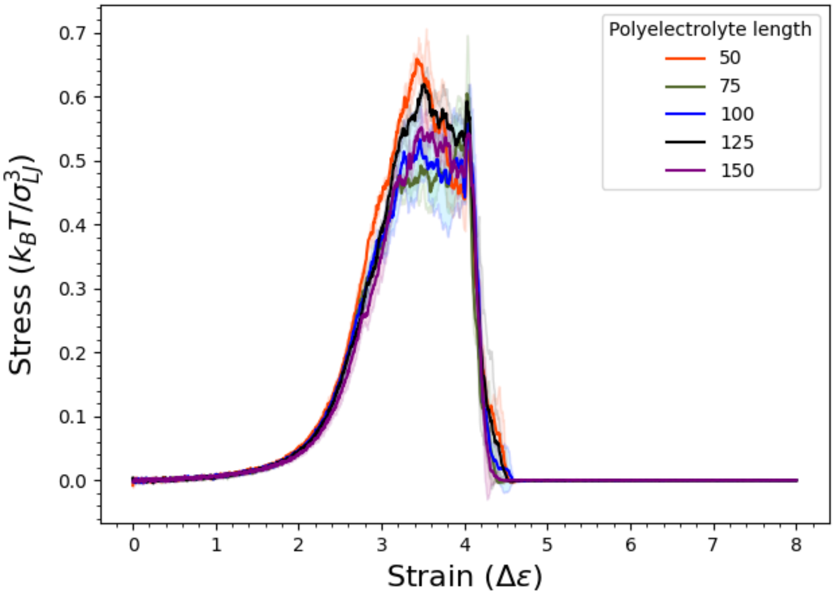

Figure 31: A continuous tensile test of different PE lengths in the same cross link density of SP. The lines indicate the average value of three replicas of the system in three different direction of strain whereas its background color indicates the errors.

Since the formation of network, especially the PE as the first network, affects the result of the tensile test, this simulation was performed in three different replicas at three different axes of x, y, and z. For instance, a system might form the collapse of PE that extends along the x-axis, a tensile test along z-axis and y-axis would show a different result than that of the x-axis. Therefore, an average result would provide better information, as is shown in Figure 31. Higher stress values are shown by the 50 PE beads. This might be addressed by the fact that the shortest PE chains collapse more than longer chains, leading to centered distribution of PE and limiting their chance of entangling with the second network. Meanwhile, the strain was applied in uniform distribution in a certain direction. It can also be seen that before reach their peaks, the longest PE of 150 beads shows fairly lowest stress. As is noted that the longest PE chain collapses twistingly along their length and have higher chance of entangling with the second network. Therefore, the rigidity of first network can be neutralized by the second network. Better visualization is shown in Figure 32.

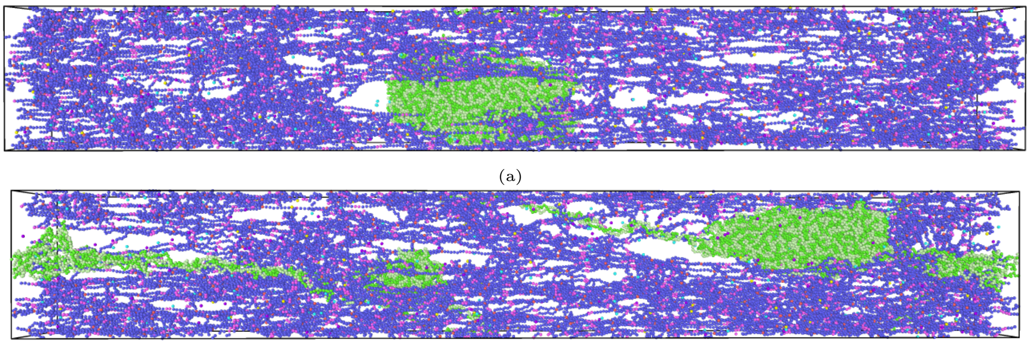

(a)

(b)

Figure 32: The snapshots of tensile test simulation at the strain $\Delta\varepsilon \approx 4$. The PE chains of 50 beads (a) are collapsed in centered distribution with less entanglement to the second network. The PE chains of 150 beads have higher chance of entangling with the second network, allowing the stress distribution to the second network during tensile test.

The fully charged chains create less space for the PE to entangle with the second network, leading to a non-uniform distribution of stress during the tensile test. In contrast, partially charged chains create more space, promoting greater entanglement with the second network. To investigate how charge fraction influences the mechanical properties, tensile tests will be conducted across samples with varying charge fractions. These tests will provide insights into how the degree of entanglement and electrostatic interactions impact stress distribution and the overall mechanical performance of the networks.

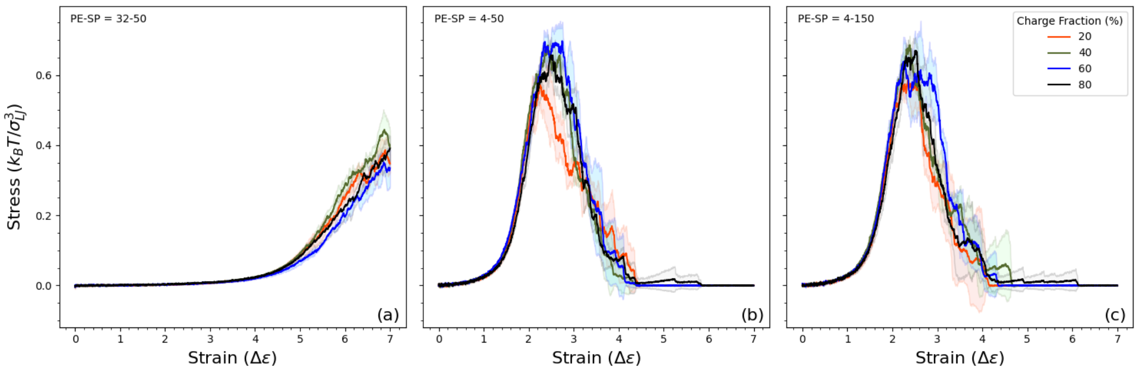

Figure 33: Tensile test of the sample with formation of SP-PE: 32-50 (a), 4-50(b), and 4-150 (c). Figures a and b provide a comparison of the tensile test results for the PE chain in the lowest and highest crosslink densities of the second network. The soft properties dominate at low crosslink density, as indicated by the stress increasing at $\Delta\varepsilon \approx 4.5$. Figures b and c provide a comparison of the tensile test results for the shortest and longest PE chains at the same crosslink density of the second network. Both samples show increasing stress at a strain of approximately $\Delta\varepsilon \approx 1.5$, but the trends after reaching their peaks are different, as the 50 beads at 20% charge fraction exhibit the bond breakage at low strain ($\Delta\varepsilon \approx 2$)

Figure 33 provide insights about the tensile test of three different samples in the different charge fractions. The effect of crosslink density is shown in the comparison of figure33 (a) and (b), agree with the fact that the rigidity of networks is increasing as the crosslink density increases as well[31]. The systems in the high crosslink density display the rupture of the network at the strain $\Delta\varepsilon \approx 2.5$, meanwhile at the strain $\Delta\varepsilon \approx 7$, there is still no sign of rupture of the samples in the low crosslink density. The tensile test comparison between the shortest and longest PE chains at different charge fractions shows no significant differences, primarily due to the high dominance of the SP network.

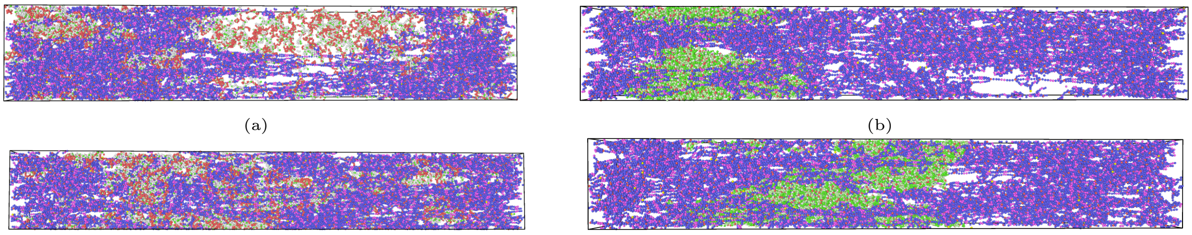

(a)

(b)

(c)

(d)

Figure 34: Snapshots of strained samples in different length of PE chain and different charge fraction. A system of 50 beads of PE with a 20% charge fraction (a) shows that concentrated PE with a lower charge fraction leads to a non-uniform distribution of stress and easier rupture. A system of 50 beads of PE with a 80% charge fraction (b), PE maintain its rigidity but less space created for entanglement. A system of 150 beads of PE with a 20% charge fraction (c) forms a more distributed complexation, but the lower charge fraction reduces its rigidity. A system of 150 beads of PE with an 80% charge fraction (d) forms a more distributed complexation, but creates less space for entanglement.

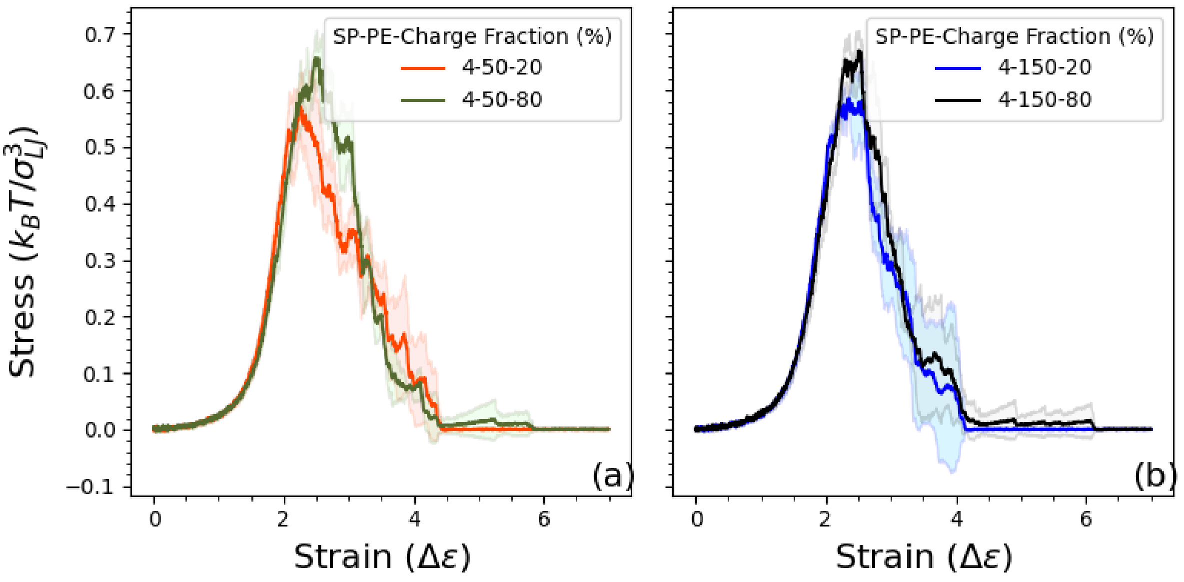

Figure 35: Tensile test of 50 beads PE (a) and 150 beads (b) in the charge fraction 20% and 80%. At 150 beads, a low charge fraction promotes an interpenetrating network, resulting in the system's survival under high stress. However, since a low charge fraction reduces the rigidity of the PE network, in the case of 50 beads, where short PE chains exhibit weak electrostatic interactions and less entanglement with the neutral network, a low charge fraction results in the gradual rupture of the network, as indicated by the decreasing stress at low strain after reaching the peak.

However, visualization reveals that the lowest charge fraction in the PE network facilitates greater entanglement with the SP network, which aligns with the expectations for ideal entanglement, is shown in Figure 34. The confirmation is shown in Figure 35. In the 150-bead system, the effect of entanglement caused by a reduced charge fraction results in the system surviving at high stress. Likewise, 150 beads with a 20% charge fraction exhibit a higher peak stress than those with an 80% charge fraction. Meanwhile, in the short PE chains, a lower charge fraction reduces the electrostatic interactions responsible for maintaining the rigidity of the PE network. As a result, a 50-bead PE chain with a 20% charge fraction did not survive under high stress and exhibited gradual bond breakage at high strain, as indicated by decreasing stress. Therefore, while increased entanglement is observed at lower charge fractions, it comes at the cost of reduced network rigidity. However, the reduced rigidity of the DN can be counterbalanced if a percolating network is formed.

5 Conclusion

This work presents different forms of complex coacervation in the double network system through coarse-grained molecular dynamics simulation. From the perspective of complex coacervate formation, polyelectrolyte (PE) chains influence the coacervation in the following way: shorter PE chains collapse more than longer chains, as the result of counterion condensation, leading to reduced electrostatic repulsion and decrease chain stretching. The degree of coacervation was measured using the OVITO surface mesh and VMD SASA, both of which show a fairly consistent increasing trend in surface area as the length of the PE chains increases. The presence of the SP network as a second network in the formation of complex coacervates is not significant, as indicated by the lack of a clear trend when the length of the SP chains was varied. It should also be noted that the noise in the trend is attributed to the fact that each system requires a different amount of time to reach an equilibrium state. The effect of charge density on PE chains was also observed, exhibiting a trend of decreasing coacervation degree as the charge fraction is reduced.

Radius of Gyration R_g of each system aligns with the theoretical calculation of R_g for ideal linear chain, in sense of longer chain have a larger R_g. However, the simulation shows a larger R_g since the conformation of the chain is influenced by both bonded and non-bonded interactions. In terms of different charge densities, the effect of reduced charge density is more pronounced in longer PE chains since they have stronger electrostatic interactions. The irregular trend of R_g for shorter chains is also attributed to the fact that, for the same total number of beads, shorter chains have more chain ends, which might disrupt charge correlation.

As shown in the MSD plot, the evolution of PE chains during equilibration reveals that shorter chains move more freely. This is due to their smaller size and weaker electrostatic interactions, which make their motions less restricted. The effect of electrostatic strength is confirmed by the MSD plot of different charge densities, which shows that PE chains with 20% charge density have higher mobility.

In terms of electrostatic interactions, the stronger interactions of longer PE chains are also confirmed by the RDF plots, which exhibit the highest density peak at shorter ranges and a steeper decline at longer ranges. Similarly, the strength of electrostatic interactions is further confirmed by the RDF plot of 80% charge density, which shows the highest first and second peaks

As a result of the constructed DN hydrogels, tensile tests were performed on systems with different charge densities. For the longest PE chain, reduced charge density promotes the formation of an interpenetrating network structure. The entanglement of the first network with the second network mitigates fracture, as the rigidity of the first network is neutralized by the softer second network. The partially charged chains create more space, promoting entanglement. However, this comes at the cost of the rigidity of the first network, as confirmed by the fact that the shortest PE chains did not survive under high stress.

References

[1] T.-C. Ho, C.-C. Chang, H.-P. Chan, T.-W. Chung, C.-W. Shu, K.-P. Chuang, T.-H. Duh, M.-H. Yang, and Y.-C. Tyan, "Hydrogels: Properties and applications in biomedicine," *Molecules*, vol. 27, no. 9, 2022.

[2] Y. Zhang, Y. Liu, J. Liu, P. Guo, and L. Heng, "Super water absorbency ommt/paa hydrogel materials with excellent mechanical properties," *RSC Adv.*, vol. 7, pp. 14504–14510, 2017.

[3] A. S. Hoffman, "Hydrogels for biomedical applications," *Advanced Drug Delivery Reviews*, vol. 64, pp. 18–23, 2012.

[4] J. P. Gong, "Why are double network hydrogels so tough," *THe Royal Society of Chemistry*, vol. 6, pp. 2583–2590, 2010.

[5] Y. Osada and M. Hasebe, "Electrically activated mechanochemical devices using polyelectrolyte gels," *Chemistry Letters*, vol. 14, pp. 1285–1288, 03 2006.

[6] Y. Osada, H. Okuzaki, and H. Hori, "A polymer gel with electrically driven motility," *Nature*, vol. 355, pp. 242–244, 1992.

[7] T. Hirai, H. Nemoto, T. Suzuki, S. Hayashi, and M. Hirai, "Actuation of poly(vinyl alcohol) gel by electric field," *Journal of Intelligent Material Systems and Structures*, vol. 4, no. 2, pp. 277–279, 1993.

[8] R. Yoshida, K. Uchida, Y. Kaneko, K. Sakai, A. Kikuchi, Y. Sakurai, and T. Okano, "Comb-type grafted hydrogels with rapid deswelling response to temperature changes," *Nature*, vol. 374, pp. 240–242, 1995.

[9] H. Xin, S. Z. Saricilar, H. R. Brown, P. G. Whitten, and G. M. Spinks, "Effect of first network topology on the toughness of double network hydrogels," *Macromolecules*, vol. 46, no. 10, pp. 6613–6620, 2013.

[10] A. J. Kerin, M. R. Wisnom, and M. A. Adams, "The compressive strength of articular cartilage," *Proceedings of the Institution of Mechanical Engineers, Part H: Journal of Engineering in Medicine*, vol. 212, no. 4, pp. 273–280, 1998. PMID: 9769695.

[11] J.-Y. Sun, X. Zhao, W. R. K. Illeperuma, O. Chaudhuri, K. H. Oh, D. J. Mooney, J. J. Vlassak, and Z. Suo, "Highly stretchable and tough hydrogels," *Nature*, vol. 489, pp. 133–136, 09 2012.

[12] K. J. Henderson, T. C. Zhou, K. J. Otim, and K. R. Shull, "Ionically cross-linked triblock copolymer hydrogels with high strength," *Macromolecules*, vol. 43, no. 14, pp. 6193–6201, 2010.

[13] D. Tuncaboylu, M. Sari, W. Oppermann, and O. Okay, "Tough and self-healing hydrogels formed via hydrophobic interactions," *Macromolecules*, vol. 44, 06 2011.

[14] S. Shams Es-haghi and R. A. Weiss, "Fabrication of tough double-network hydrogels from highly cross-linked brittle neutral networks using alkaline hydrolysis," *Gels*, vol. 10, no. 1, 2024.

[15] Y. Zheng, Y. Wang, F. Tian, T. Nakajima, C.-Y. Hui, and J. P. Gong, "Unique stick–slip crack dynamics of double-network hydrogels under pure-shear loading,"

Proceedings of the National Academy of Sciences, vol. 121, no. 30, p. e2322437121, 2024.

[16] E. A. Appel, J. del Barrio, X. J. Loh, and O. A. Scherman, “Supramolecular polymeric hydrogels,” *Chem. Soc. Rev.*, vol. 41, pp. 6195–6214, 2012.

[17] B. Sim, J. J. Chang, Q. Lin, J. H. M. Wong, V. Ow, Y. Leow, Y. J. Wong, Y. J. Boo, R. Goh, and X. J. Loh, “Hydrogels based on polyelectrolyte complexes: Underlying principles and biomedical applications,” *Biomacromolecules*, vol. 25, no. 12, pp. 7563–7580, 2024.

[18] F. Luo, T. L. Sun, T. Nakajima, T. Kurokawa, Y. Zhao, K. Sato, A. B. Ihsan, X. Li, H. Guo, and J. P. Gong, “Oppositely charged polyelectrolytes form tough, self-healing, and rebuildable hydrogels,” *Advanced Materials*, vol. 27, no. 17, pp. 2722–2727, 2015.

[19] M. Malkoch, R. Vestberg, N. Gupta, L. Mespouille, P. Dubois, A. F. Mason, J. L. Hedrick, Q. Liao, C. W. Frank, K. Kingsbury, and C. J. Hawker, “Synthesis of well-defined hydrogel networks using click chemistry,” *Chem. Commun.*, pp. 2774–2776, 2006.

[20] G. Lalevée, L. David, A. Montembault, K. Blanchard, J. Meadows, S. Malaise, A. Crépet, I. Grillo, I. Morfin, T. Delair, and G. Sudre, “Highly stretchable hydrogels from complex coacervation of natural polyelectrolytes,” *Soft Matter*, vol. 13, pp. 6594–6605, 2017.

[21] Y. Wu, Y. Nie, Z. Long, P. Si, and D. Zhang, “Coacervation-based method for constructing a multifunctional strain-stiffening crystalline polyvinylamine hydrogel,” *ACS Applied Materials & Interfaces*, vol. 14, no. 27, pp. 31354–31362, 2022.

[22] S. Y. Joshi and S. A. Deshmukh, “A review of advancements in coarse-grained molecular dynamics simulations,” *Molecular Simulation*, vol. 47, no. 10-11, pp. 786–803, 2021.

[23] M. G. Saunders and G. A. Voth, “Coarse-graining methods for computational biology,” *Annual Review of Biophysics*, vol. 42, no. Volume 42, 2013, pp. 73–93, 2013.

[24] J. E. Sayed, A. Mukherjee, S. E. Aani, N. Vengallur, M. Koch, A. Giuntoli, and M. Kamperman, “Structureproperty relationships of granular hybrid hydrogels formed through polyelectrolyte complexation,” *Macromolecules*, vol. 57, no. 7, pp. 3190–3207, 2024.

[25] Q. Chai and X. Yu, “Hydrogels for biomedical applications: Their characteristic and the mechanism behind them,” *gels*, vol. 3, no. 6, 2017.

[26] S. Bashir, M. Hina, J. Iqbal, A. H. Rajpar, M. A. Mujtaba, N. A. Alghamdi, S. Wageh, K. Ramesh, and S. Ramesh, “Fundamental concepts of hydrogels: Synthesis, properties, and their applications,” *Polymers*, vol. 12, no. 11, 2020.

[27] M. Bustamante-Torres, D. Romero-Fierro, B. Arcentales-Vera, K. Palomino, H. Magaña, and E. Bucio, “Hydrogels classification according to the physical or chemical interactions and as stimuli-sensitive materials,” *Gels*, vol. 7, no. 4, 2021.

[28] S. Tang, L. Zhao, J. Yuan, Y. Chen, and Y. Leng, “Chapter 3 - physical hydrogels based on natural polymers,” in *Hydrogels Based on Natural Polymers* (Y. Chen, ed.), pp. 51–89, 2020.

[29] H. Tsukeshiba, M. Huang, Y.-H. Na, T. Kurokawa, R. Kuwabara, Y. Tanaka, H. Furukawa, Y. Osada, and J. P. Gong, “Effect of polymer entanglement on the toughening of double network hydrogels,” *The Journal of Physical Chemistry B*, vol. 109, no. 24, pp. 16304–16309, 2005.

[30] J. Gong, Y. Katsuyama, T. Kurokawa, and Y. Osada, “Double-network hydrogels with extremely high mechanical strength,” *Advanced Materials*, vol. 15, no. 14, pp. 1155–1158, 2003.

[31] T. Nakajima, H. Furukawa, Y. Tanaka, T. Kurokawa, Y. Osada, and J. P. Gong, “True chemical structure of double network hydrogels,” *Macromolecules*, vol. 42, no. 6, pp. 2184–2189, 2009.

[32] M. Huang, H. Furukawa, Y. Tanaka, T. Nakajima, Y. Osada, and J. P. Gong, “Importance of entanglement between first and second components in high-strength double network gels,” *Macromolecules*, vol. 40, no. 18, pp. 6658–6664, 2007.

[33] T. Tominaga, V. R. Tirumala, E. K. Lin, J. P. Gong, H. Furukawa, Y. Osada, and W. li Wu, “The molecular origin of enhanced toughness in double-network hydrogels: A neutron scattering study,” *Polymer*, vol. 48, no. 26, pp. 7449–7454, 2007.

[34] H. R. Brown, “A model of the fracture of double network gels,” *Macromolecules*, vol. 40, no. 10, pp. 3815–3818, 2007.

[35] T. Nakajima and J. P. Gong, *Double-Network Hydrogels: Soft and Tough IPN*, pp. 1–6. Berlin, Heidelberg: Springer Berlin Heidelberg, 2021.

[36] C. Creton, “50th anniversary perspective: Networks and gels: Soft but dynamic and tough,” *Macromolecules*, vol. 50, no. 21, pp. 8297–8316, 2017.

[37] J. P. Gong, “Materials both tough and soft,” *Science*, vol. 344, no. 6180, pp. 161–162, 2014.

[38] M. Rubinstein and R. H. Colby, *Polymer physics*. Oxford university press, 2003.

[39] L. R. G. Treloar, “The elasticity and related properties of rubbers,” *Reports on Progress in Physics*, vol. 36, pp. 755–826, 1973.

[40] M. Rubinstein and S. Panyukov, “Nonaffine deformation and elasticity of polymer networks,” *Macromolecules*, vol. 30, no. 25, pp. 8036–8044, 1997.

[41] F. Lu, T. Nakajima, Y. Zheng, H. Fan, and J. P. Gong, “Tensile behaviors of double network hydrogels with varied first network topological and chemical structures,” *Macromolecules*, vol. 57, no. 24, pp. 11520–11533, 2024.

[42] K. Saito, T. Sakai, J. P. Gong, and M. Kubo, “Fracture process of double-network gels by coarse-grained molecular dynamics simulation,” *Macromolecules*, vol. 51, no. 8, pp. 3075–3087, 2018.

[43] C. E. Sing and S. L. Perry, “Recent progress in the science of complex coacervation,” *Soft Matter*, vol. 16, pp. 2885–2914, 2020.

[44] Y. P. Timilsena, T. O. Akanbi, N. Khalid, B. Adhikari, and C. J. Barrow, “Complex coacervation: Principles, mechanisms and applications in microencapsulation,” *International Journal of Biological Macromolecules*, vol. 121, pp. 1276–1286, 2019.

[45] Y. Lin, J. McCarty, J. N. Rauch, K. T. Delaney, K. S. Kosik, G. H. Fredrickson, J.-E. Shea, and S. Han, “Narrow equilibrium window for complex coacervation of tau and rna under cellular conditions,” *Elife*, vol. 8, p. e42571, 2019.

[46] J. T. G. Overbeek and M. J. Voorn, “Phase separation in polyelectrolyte solutions. theory of complex coacervation,” *Journal of Cellular and Comparative Physiology*, vol. 49, no. S1, pp. 7–26, 1957.

[47] P. Debye and E. Hückel, “On the theory of electrolytes. i. freezing point depression and related phenomena,” *Phys. Z*, vol. 24, pp. 185–206, 1923.

[48] D. McQuarrie, “Statistical mechanics university science,” *Sausalito, CA*, pp. 222–223, 2000.

[49] S. L. Perry, Y. Li, D. Priftis, L. Leon, and M. Tirrell, “The effect of salt on the complex coacervation of vinyl polyelectrolytes,” *Polymers*, vol. 6, no. 6, pp. 1756–1772, 2014.

[50] E. Spruijt, A. H. Westphal, J. W. Borst, M. A. Cohen Stuart, and J. van der Gucht, “Binodal compositions of polyelectrolyte complexes,” *Macromolecules*, vol. 43, no. 15, pp. 6476–6484, 2010.

[51] A. A. André and E. Spruijt, “Liquid–liquid phase separation in crowded environments,” *International Journal of Molecular Sciences*, vol. 21, no. 16, p. 5908, 2020.

[52] Q. Bai, Z. Liu, J. Chen, and D. Liang, “Crowded environment regulates the coacervation of biopolymers via nonspecific interactions,” *Biomacromolecules*, vol. 24, no. 1, pp. 283–293, 2022.

[53] D. V. Krogstad, N. A. Lynd, S.-H. Choi, J. M. Spruell, C. J. Hawker, E. J. Kramer, and M. V. Tirrell, “Effects of polymer and salt concentration on the structure and properties of triblock copolymer coacervate hydrogels,” *Macromolecules*, vol. 46, no. 4, pp. 1512–1518, 2013.

[54] J. N. Hunt, K. E. Feldman, N. A. Lynd, J. Deek, L. M. Campos, J. M. Spruell, B. M. Hernandez, E. J. Kramer, and C. J. Hawker, “Tunable, high modulus hydrogels driven by ionic coacervation,” *Advanced Materials*, vol. 23, no. 20, pp. 2327–2331, 2011.

[55] M. Zhang, Y. Yang, M. Li, Q. Shang, R. Xie, J. Yu, K. Shen, Y. Zhang, and Y. Cheng, “Toughening double-network hydrogels by polyelectrolytes,” *Advanced Materials*, vol. 35, no. 26, p. 2301551, 2023.

[56] R. H. Landau, M. J. Páez, and C. C. Bordeianu, *Computational physics: Problem solving with Python.* John Wiley & Sons, 2024.

[57] J. Salacuse, A. Denton, and P. Egelstaff, “Finite-size effects in molecular dynamics simulations: Static structure factor and compressibility. i. theoretical method,” *Physical Review E*, vol. 53, no. 3, p. 2382, 1996.

[58] C. G. Jesudason, "Simulation algorithm that conserves energy and momentum for molecular dynamics of systems driven by switching potentials," *Mathematical Problems in Engineering*, vol. 2009, no. 1, p. 215815, 2009.

[59] M. Dallavalle and N. F. van der Vegt, "Evaluation of mapping schemes for systematic coarse graining of higher alkanes," *Physical Chemistry Chemical Physics*, vol. 19, no. 34, pp. 23034–23042, 2017.

[60] D. Fritz, V. A. Harmandaris, K. Kremer, and N. F. Van Der Vegt, "Coarse-grained polymer melts based on isolated atomistic chains: Simulation of polystyrene of different tacticities," *Macromolecules*, vol. 42, no. 19, pp. 7579–7588, 2009.

[61] S. J. Marrink, H. J. Risselada, S. Yefimov, D. P. Tieleman, and A. H. De Vries, "The martini force field: coarse grained model for biomolecular simulations," *The journal of physical chemistry B*, vol. 111, no. 27, pp. 7812–7824, 2007.

[62] J. Zhang, H. Zhang, T. Wu, Q. Wang, and D. Van Der Spoel, "Comparison of implicit and explicit solvent models for the calculation of solvation free energy in organic solvents," *Journal of chemical theory and computation*, vol. 13, no. 3, pp. 1034–1043, 2017.

[63] C. Peter, L. Delle Site, and K. Kremer, "Classical simulations from the atomistic to the mesoscale and back: coarse graining an azobenzene liquid crystal," *Soft Matter*, vol. 4, no. 4, pp. 859–869, 2008.

[64] C. F. Abrams and K. Kremer, "Effects of excluded volume and bond length on the dynamics of dense bead-spring polymer melts," *The Journal of chemical physics*, vol. 116, no. 7, pp. 3162–3165, 2002.

[65] D. Kauzlarić, J. T. Meier, P. Español, S. Succi, A. Greiner, and J. G. Korvink, "Bottom-up coarse-graining of a simple graphene model: The blob picture," *The Journal of chemical physics*, vol. 134, no. 6, 2011.

[66] M. E. Johnson, T. Head-Gordon, and A. A. Louis, "Representability problems for coarse-grained water potentials," *The Journal of chemical physics*, vol. 126, no. 14, 2007.

[67] N. J. Dunn and W. Noid, "Bottom-up coarse-grained models that accurately describe the structure, pressure, and compressibility of molecular liquids," *The Journal of chemical physics*, vol. 143, no. 24, 2015.

[68] P. M. Morse, "Diatomic molecules according to the wave mechanics. ii. vibrational levels," *Phys. Rev.*, vol. 34, pp. 57–64, Jul 1929.

[69] K. Kremer and G. S. Grest, "Dynamics of entangled linear polymer melts: A molecular-dynamics simulation," *American Institute of Phyics*, vol. 92, no. 5057, 1990.

[70] A. Y. Shih, A. Arkhipov, P. L. Freddolino, and K. Schulten, "Coarse grained protein-lipid model with application to lipoprotein particles," *The Journal of Physical Chemistry B*, vol. 110, no. 8, pp. 3674–3684, 2006.

[71] J. P. Dürholt, R. Galvelis, and R. Schmid, "Coarse graining of force fields for metal–organic frameworks," *Dalton Transactions*, vol. 45, no. 10, pp. 4370–4379, 2016.

[72] W. Hu, *Polymer physics: a molecular approach.* Springer Science & Business Media, 2012.

[73] R. W. Hockney and J. W. Eastwood, *Computer simulation using particles.* crc Press, 2021.

[74] H. Song and M. I. Mendelev, "Molecular dynamics simulation of phase competition in terbium," *The Journal of Chemical Physics*, vol. 149, no. 24, p. 244501, 2018.

[75] A. L. Melchor, C. Camas, F. R. Gonzalez, and H. Vilchis, "Molecular dynamics to model carbon infiltration into a porous silicon matrix: An experimental and computational approach," *Computational Materials Science*, vol. 238, p. 112949, 2024.

[76] O. R. Deluigi, F. Valencia, N. Amigo, F. Aquistapace, R. I. Gonzalez, and E. M. Bringa, "Atomistic simulations of tensile deformation of a nanoporous high-entropy alloy," *Journal of Materials Science*, vol. 57, no. 42, pp. 19817–19831, 2022.

[77] H. Edelsbrunner and E. P. Mucke, "Three-dimensional alpha shapes," *ACM Transactions on Graphics*, vol. 13, no. 1, pp. 43–72, 1994.

[78] G. Taubin, "Geometric signal processing on polygonal meshes," *SIGGRAPH*, vol. 95, pp. 351–358, 1995.

[79] B. D. Dice, V. Ramasubramani, E. S. Harper, M. P. Spellings, J. A. Anderson, and S. C. Glotzer, "Analyzing particle systems for machine learning and data visualization with freud," in *Proceedings of the 18th Python in Science Conference* (C. Calloway, D. Lippa, D. Niederhut, and D. Shupe, eds.), pp. 27–33, 2019.

[80] Richard J. Gowers, Max Linke, Jonathan Barnoud, Tyler J. E. Reddy, Manuel N. Melo, Sean L. Seyler, Jan Domański, David L. Dotson, Sébastien Buchoux, Ian M. Kenney, and Oliver Beckstein, "MDAnalysis: A Python Package for the Rapid Analysis of Molecular Dynamics Simulations," in *Proceedings of the 15th Python in Science Conference* (Sebastian Benthall and Scott Rostrup, eds.), pp. 98 – 105, 2016.

[81] N. Michaud-Agrawal, E. J. Denning, T. B. Wolf, and O. Beckstein, "Mdanalysis: a toolkit for the analysis of molecular dynamics simulations," *Journal of Computational Chemistry*, vol. 32, no. 10, pp. 2319–2327, 2011.

[82] A. Stutowski, "Computational analysis methods in atomistic modeling of crystals," *JOM*, vol. 66, no. 3, pp. 399–407, 2014.

[83] N. V. Brilliantov, D. V. Kuznetsov, and R. Klein, "Chain collapse and counterion condensation in dilute polyelectrolyte solutions," *Phys. Rev. Lett.*, vol. 81, pp. 1433–1436, Aug 1998.

[84] B.-Y. Ha and D. Thirumalai, "Conformations of a polyelectrolyte chain," *Physical Review A*, vol. 46, no. 6, p. R3012, 1992.

[85] S. Chen and Z.-G. Wang, "Driving force and pathway in polyelectrolyte complex coacervation," *Proceedings of the National Academy of Sciences*, vol. 119, no. 36, p. e2209975119, 2022.

[86] S. M. Lalwani, P. Batys, M. Sammalkorpi, and J. L. Lutkenhaus, "Relaxation times of solid-like polyelectrolyte complexes of varying ph and water content," *Macromolecules*, vol. 54, no. 17, pp. 7765–7776, 2021.

[87] A. Zintchenko, G. Rother, and H. Dautzenberg, "Transition highly aggregated complexessoluble complexes via polyelectrolyte exchange reactions: kinetics, structural changes, and mechanism," *Langmuir*, vol. 19, no. 6, pp. 2507–2513, 2003.

[88] B. Lee and F. Richards, "The interpretation of protein structures: Estimation of static accessibility," *Journal of Molecular Biology*, vol. 55, no. 5, pp. 379–405, 1971.

[89] Y. Ma, S. Velioğlu, Z. Yin, R. Wang, and J. W. Chew, "Molecular dynamics investigation of membrane fouling in organic solvents," *Journal of Membrane Science*, vol. 632, p. 119329, 2021.

[90] H. Chen and A. Z. Panagiotopoulos, "Molecular modeling of surfactant micellization using solvent-accessible surface area," *Langmuir*, vol. 35, no. 6, pp. 2443–2450, 2019.

[91] M. Nierlich, F. Boue, A. Lapp, and R. Oberthur, "Radius of gyration of polyion in salt free polyelectrolyte solutions measured by s.a.n.s.," *Journal de Physique*, vol. 46, no. 4, pp. 649–655, 1985.

[92] P.-Y. Hsiao and E. Luijten, "Salt-induced collapse and reexpansion of highly charged flexible polyelectrolytes," *Phys. Rev. Lett*, vol. 97, no. 14, p. 148301, 2006.

[93] S. Mitra and A. Kundagrami, "Polyelectrolyte complexation of two oppositely charged symmetric polymers: A minimal theory," *The Journal of Chemical Physics*, vol. 158, no. 1, p. 014904, 2023.

[94] V. Milkova and T. Radeva, "Effect of chain length and charge density on the construction of polyelectrolyte multilayers on colloidal particles," *Journal of colloid and interface science*, vol. 308, no. 3, p. 300–308, 2007.

[95] K. Shen and Z.-G. Wang, "Polyelectrolyte chain structure and solution phase behavior," *Macromolecules*, vol. 51, no. 5, p. 1706–1717, 2018.

[96] Y. D. Gordievskaya, A. A. Gavrilov, and E. Y. Kramarenko, "Effect of counterion excluded volume on the conformational behavior of polyelectrolyte chains," *Soft Matter*, vol. 14, no. 8, p. 1474–1481, 2018.

[97] D. Fragiadakis and C. M. Roland, "Chain flexibility and the segmental dynamics of polymers," *The Journal of Physical Chemistry B*, vol. 123, no. 27, p. 5930–5934, 2019.

[98] W. C. Soysa, B. Dünweg, and J. R. Prakash, "Size, shape, and diffusivity of a single debye-hückel polyelectrolyte chain in solution," *The Journal of Physical Chemistry*, vol. 143, no. 6, pp. 1089–7690, 2015.

[99] K. Radhakrishnan and S. P. Singh, "Explicit characterization of counterion dynamics around a flexible polyelectrolyte," *Phys. Rev. E*, vol. 105, no. 4, p. 044501, 2022.

[100] T. Zhou and S. B. Chen, “Computer simulations of diffusion and dynamics of short-chain polyelectrolytes,” *The Journal of Physical Chemistry*, vol. 124, no. 3, p. 034904, 2006.

[101] M. Quesada-Pérez, I. Adroher-Benítez, and J. A. Maroto-Centeno, “Size-exclusion partitioning of neutral solutes in crosslinked polymer networks: A monte carlo simulation study,” *The Journal of Chemical Physics*, vol. 140, no. 20, p. 204910, 2014.

[102] M. Zhang, D. Zhang, H. Chen, Y. Zhang, Y. Liu, B. Ren, and J. Zheng, “A multiscale polymerization framework towards network structure and fracture of double-network hydrogels,” *npj Computational Materials*, vol. 7, no. 1, p. 39, 2021.

[103] R. Zandi, J. Rudnick, and R. Golestanian, “Radial distribution function of rod-like polyelectrolytes,” *The European Physical Journal E*, vol. 9, no. 1, pp. 41–46, 2002.

[104] R. Zandi, J. Rudnick, and R. Golestanian, “Probing polyelectrolyte elasticity using radial distribution function,” *The European Physical Journal E*, vol. 67, no. 2, 2003.

[105] A. Malovikova, K. Hayakawa, and J. C. T. Kwak, “Surfactant-polyelectrolyte interactions. 4. surfactant chain length dependence of the binding of alkylpyridinium cations to dextran sulfate,” *The Journal of Physical Chemistry*, vol. 88, no. 10, pp. 1930–1933, 1984.

[106] J. C. Chu and C. H. Mak, “Inter- and intrachain attractions in solutions of flexible polyelectrolytes at nonzero concentration,” *The Journal of Chemical Physics*, vol. 110, no. 5, pp. 2669–2679, 1999.

[107] S. E. Prameela, C. C. Walker, C. S. DiMarco, D. D. Mallick, X. Sun, S. Hernandez, T. Sasaki, J. W. Wilkerson, K. T. Ramesh, G. M. Pharr, and T. P. Weihs, “Rapid quantification of dynamic and spall strength of metals across strain rates,” 2023.

[108] A. Drozdov and J. deClaville Christiansen, “Mechanical response of double-network gels with dynamic bonds under multi-cycle deformation,” *Polymer*, vol. 150, pp. 95–108, 2018.